J. Fluid Mech. (1994), *vol.* 264, *pp.* 1–40

Wavenumber selection and irregularity of spatially developing nonlinear Dean and Görtler vortices

By Y. GUO† AND W. H. FINLAY

Department of Mechanical Engineering, University of Alberta, Edmonton, Alberta, Canada, T6G 2G8

(Received 11 April 1992 and in revised form 9 September 1993)

Spatially developing vortices found in curved channels (Dean vortices) and in a concave boundary layer (Görtler vortices) asre studied numerically using Legendre spectral-element methods. The linear instability of these vortices with respect to spanwise perturbations (Eckhaus instability) is examined using parabolized spatial stability analysis. The nonlinear evolution of this instability is studied by solving the parabolized Navier–Stokes equations. When the energy level of Dean and Görtler vortices in the flow is low, the spatial growth of the vortices is governed by primary instability (Dean or Görtler instability). At this stage, vortices with different wavelengths can develop at the same time and do not interact with each other significantly. When certain vortices reach the nonlinear stage first and become the dominant wavelength, spatial Eckhaus instability sets in. For all cases studied, spatially developing Dean and Görtler vortices are found to be most unstable to spanwise disturbances with wavelength twice or $\frac{3}{2}$ times that of the dominant one. The nonlinear growth of these perturbations generates a small vortex pair in between two pairs of vortices with long wavelength, but forces two pairs of vortices with short wavelength to develop into one pair. For Görtler vortices, this is manifested mostly by irregular and deformed vortex structures. For Dean vortices, this is manifested by vortex splitting and merging, and spatial Eckhaus instability plays an important role in the wavenumber selection process.

1. Introduction

Counter-rotating streamwise vortices caused by streamwise curvature have been attracting many researchers' attention for years. They can be found in many applications and play an important role in the transition toward turbulence. For open fluid systems where fluid particles are advected through the system, Dean vortices found in curved channels (Dean 1928) and Görtler vortices near a concave surface (Görtler 1940) are two classical examples of such vortices. Since these vortices significantly change the flow pattern, the boundary-layer structure, and the transition to turbulence, a better understanding of these vortices may lead to a better understanding of many flows including the flows near the concave surfaces of turbine blades and aerofoils, and coolant flows inside turbine blades. Because of the analogies between the effects of curvature, rotation and buoyancy, the study of Dean vortices and Görtler vortices may also give some insight into the effects of rotation and buoyancy on transitions in the flow on a rotating plate and inside a rotating channel. In this study, using a Legendre spectral-element method and spatial instability theory,

† Present address: DLR, Institute for Theoretical Fluid Mechanics, Bunsenstrasse 10, D-37073 Göttingen, Germany.

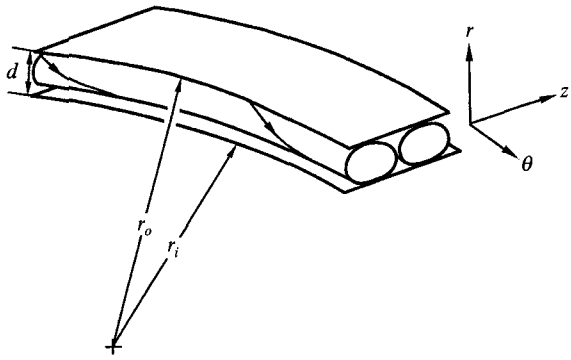

FIGURE 1. The geometry of curved channel flow.

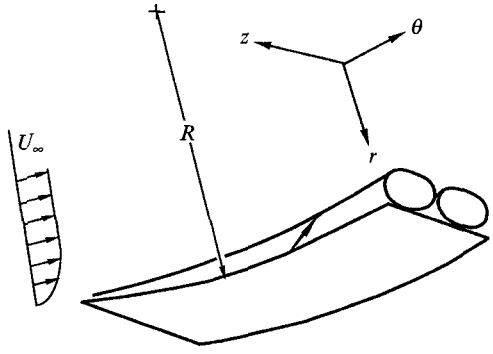

FIGURE 2. The geometry of boundary layer flow over a concave surface. The streamwise direction is θ.

we examine numerically the instabilities of Dean and Görtler vortices with respect to spanwise perturbations and the effects of these perturbations on wavenumber selection and nonlinear development of these vortices.

The flow geometries for Dean and Görtler vortices are shown in figures 1 and 2. The streamwise and spanwise directions of the flow are given by θ and z respectively. For Dean vortices the channel spacing is $d = r_o - r_i$. The Reynolds number is $Re = \bar{U}d/2\nu$, where $\bar{U}$ is the mean (bulk) streamwise velocity. The radius ratio of the two walls is $\gamma = r_i/r_o$, which is a measure of channel curvature. The spanwise dimensionless wavenumber of the vortices is defined as $\alpha = \pi d/\lambda$, where λ is the dimensional wavelength of the vortices.

For Görtler vortices, we will restrict ourselves to the case of constant wall curvature, i.e. the radius of the wall R is constant. The free-stream velocity is U_∞. The effect of the wall curvature is measured by the Görtler number

$$G = \frac{U_\infty \delta_m}{\nu}\left(\frac{\delta_m}{R}\right)^{\frac{1}{2}},$$

where δ_m is the momentum thickness of a Blasius boundary layer at the downstream distance $x = R\theta$ from the leading edge. The wall curvature can also be measured by the ratio $\gamma = (R - \delta_{0.99})/R$, where $\delta_{0.99}$ is the Blasius boundary-layer thickness at $u_\theta = 0.99U_\infty$. In this study, the wavelength of Görtler vortices is measured by the dimensionless parameter

$$\Lambda = \frac{U_\infty \lambda}{\nu}\left(\frac{\lambda}{R}\right)^{\frac{1}{2}},$$

where λ is the dimensional wavelength in the spanwise direction. Both A and λ are constant in the streamwise direction, but G increases with boundary-layer thickness downstream.

Ever since Dean (1928) and Görtler (1940) predicted the existence of a secondary vortex-type motion in curved channels and boundary layers over concave surfaces, numerous efforts have been made both experimentally and theoretically toward an understanding of these vortices. For brevity we shall not review these studies here. Readers are referred to Finlay, Keller & Ferziger (1988), Ligrani & Niver (1988), Matsson & Alfredsson (1990, 1992), Yang & Kim (1991) and Ligrani *et al.* (1992) for some recent efforts on Dean vortices. A review of early theoretical works on Görtler vortices can be found in Herbert (1976). Owing to the difficulties associated with the non-parallel nature of the Görtler problem, there have been many controversies, and discrepancies still exist even among some recent works. Readers are referred to Floryan & Saric (1984), Day, Herbert & Saric (1990), Sabry & Liu (1991), Liu & Domaradzki (1990), Yu & Liu (1991), Lee & Liu (1992), and especially the papers from Hall and his group (e.g. 1983, 1988, 1990) for some recent theoretical efforts. For experimental works, readers are referred to Bippes (1972), Aihara & Koyama (1980), Aihara, Tomita & Ito (1984) and Swearingen & Blackwelder (1987).

To our knowledge, most previous research in the Dean and Görtler problems has dealt with primary instabilities (Dean or Görtler instability), secondary instabilities with respect to streamwise disturbances (which leads to wavy or horseshoe types of vortices), nonlinear evolutions of these vortices and the interactions of Dean or Görtler instabilities with Tollmien–Schlichting waves or other instabilities. Though many instabilities predicted by theoretical works over the years have been observed in experiments, many of the rich features revealed experimentally are still unexplained. In particular, the instabilities of spatially developing, nonlinear Dean or Görtler vortices with respect to spanwise disturbanes have never been addressed before. In Guo & Finlay (1991), we studied the instability of stationary nonlinear Dean vortices with respect to spanwise perturbation using a temporal theory. It is found that the stability boundary of such an instability is a closed loop in an (Re, α)-plane. Outside the stability boundary, the most unstable wavenumber is usually half or one and half that of the base Dean vortices. The nonlinear development of these most unstable spanwise perturbations causes two pairs of Dean vortices to split into three pairs if the wavenumbers of the vortices are small and to merge into one pair if the wavenumbers are large. We referred to this type of instability as Eckhaus instability to credit the first work of this kind done by Eckhaus (1965).

One drawback of temporal theories is the difficulty in comparing with spatially developing experimental observations. In this study, we instead use spatial instability theory and three-dimensional numerical simulation to develop a numerical method for studying the spatial Eckhaus instability and its nonlinear evolution. We examine the roles of primary instability and spatial Eckhaus instability in the wavenumber selection process and their effects on the nonlinear evolution of Dean and Görtler vortices. We believe that such a study is essential to a better understanding of the dynamics of Dean and Görtler vortices. Since both Görtler vortices and Dean vortices are caused by streamwise curvature due to centrifugal instabilities and share various similarities, we compare and contrast the features of these two types of vortices. In §2 we describe the theories and numerical approahes used in this study. Code verifications are given in §3. The linear spatial Eckhaus instability of nonlinear Dean and Görtler vortices is studied in §4. The nonlinear aspect of this instability and its effect on the wavenumber selection are discussed in §§5 and 6. Concluding remarks are given in §7.

2. Theory and numerical methods

Heuristically, one can say that when an incompressible flow has a dominant streamwise velocity and has slow streamwise variation compared with cross-stream variation, the upstream influence of downstream disturbances can be neglected and the flow has a parabolic nature in the streamwise direction. The governing Navier–Stokes equations then can be 'parabolized'. This idea has been explored rather extensively in engineering applications for many years. Readers are referred to Fletcher (1988) for a review. Recently, this approach has been employed in stability theory first by Hall (1983, 1988) for Görtler instability and by Bertolotti, Herbert & Spalart (1992) for a more general case. In this section, we first present our formulation in the frame of a parabolization approach, and then present our numerical methods to solve the resulting equations.

2.1. *Governing equations for base flow*

In this study, the base flow $\boldsymbol{u}^0$ is three-dimensional spatially developing nonlinear Dean or Görtler vortices. It has been shown by Hall (1983, 1988) that in the limit of $Re \to \infty$, Görtler vortices can be described by a set of parabolic equations derived from the Navier–Stokes equations. For curved channel flows, it has been shown both numerically and experimentally (cf. Bara, Nandakumar & Masiliyah 1992) that Dean vortices can also be described by a parabolized version of Navier–Stokes equations. In this study, we adopt the same version of the parabolized Navier–Stokes equations (PNS) used by Bara *et al.* (1992): the streamwise diffusion terms are neglected and the pressure influence on the streamwise momentum equation is considered to be invariant in the cross-stream plane, i.e. the pressure in the streamwise momentum equation is averaged over the cross-stream plane. This version of PNS can be derived through a simple scale analysis and its variations have been explored extensively by many researchers (cf. Fletcher 1988). When the radius ratio $\gamma > 0.9$, this version of PNS can be applied safely. In this study, for ease of implementation, the computational variables for the velocities are chosen to be $\phi_r = ru_r^0$, $\phi_\theta = ru_\theta^0$ and $\phi_z = ru_z^0$. The resulting PNS in cylindrical coordinates are carefully arranged in the streamwise direction as

$$2\frac{\phi_\theta}{r^3}\frac{\partial\phi_\theta}{\partial\theta}+\frac{\partial}{\partial r}\left(\frac{\phi_r\phi_\theta}{r^2}\right)+\frac{\partial}{\partial z}\left(\frac{\phi_z\phi_\theta}{r^2}\right)+\frac{2\phi_r\phi_\theta}{r^3}-\frac{1}{Re}\frac{2}{r^3}\frac{\partial\phi_r}{\partial\theta}$$
$$=-\frac{1}{r}\frac{\partial\bar{p}^0}{\partial\theta}+\frac{1}{Re}\left[\frac{\partial}{\partial r}\frac{1}{r}\frac{\partial\phi_\theta}{\partial r}+\frac{\partial}{\partial z}\frac{1}{r}\frac{\partial\phi_\theta}{\partial z}\right], \quad (2.1)$$

and in the cross-stream directions as

$$\frac{\partial}{\partial\theta}\left(\frac{\phi_\theta}{r^3}\phi_r\right)+\frac{\partial}{\partial r}\left(\frac{\phi_r\phi_r}{r^2}\right)+\frac{\partial}{\partial z}\left(\frac{\phi_z\phi_r}{r^2}\right)+\frac{(\phi_r^2-\phi_\theta^2)}{r^3}+\frac{1}{Re}\frac{2}{r^3}\frac{\partial\phi_\theta}{\partial\theta}$$
$$=-\frac{\partial p^0}{\partial r}+\frac{1}{Re}\left[\frac{\partial}{\partial r}\frac{1}{r}\frac{\partial\phi_r}{\partial r}+\frac{\partial}{\partial z}\frac{1}{r}\frac{\partial\phi_r}{\partial z}\right], \quad (2.2a)$$

$$\frac{\partial}{\partial\theta}\left(\frac{\phi_\theta}{r^3}\phi_z\right)+\frac{\partial}{\partial r}\left(\frac{\phi_r\phi_z}{r^2}\right)+\frac{\partial}{\partial z}\left(\frac{\phi_z\phi_z}{r^2}\right)+\frac{\phi_z\phi_r}{r^3}-\frac{1}{Re}\frac{\phi_z}{r^3}$$
$$=-\frac{\partial p^0}{\partial z}+\frac{1}{Re}\left[\frac{\partial}{\partial r}\frac{1}{r}\frac{\partial\phi_z}{\partial r}+\frac{\partial}{\partial z}\frac{1}{r}\frac{\partial\phi_z}{\partial z}\right]. \quad (2.2b)$$

The continuity equation is

$$-\frac{\partial\phi_r}{\partial r}-\frac{\partial\phi_z}{\partial z}=\frac{1}{r}\frac{\partial\phi_\theta}{\partial\theta}. \quad (2.3)$$

In (2.1), $\bar{p}^0$ is the pressure averaged across the (r, z)-plane. For channel flows, the velocity $\boldsymbol{u}^0$ is non-dimensionalized by the mean streamwise velocity $\bar{U}$. For growing boundary layers, $\boldsymbol{u}^0$ is non-dimensionalized by the free-stream velocity U_∞. In an (r, z)-plane, (2.1)–(2.3) are elliptic. In the streamwise direction, the variable θ behaves like time t in a two-dimensional Navier–Stokes problem. Non-slip boundary conditions are used at walls. In the spanwise direction, z, periodic boundary conditions are used for both Dean and Görtler vortices. In the case of boundary-layer flow on a concave wall, homogeneous Neumann boundary conditions are applied in the r-direction far away from the wall.

We have few comments to make about (2.1)–(2.3).

(*a*) In the limit of $R \to \infty$ (or $\gamma \to 1$) and $Re \to \infty$, only the curvature-induced term ϕ_θ^2/r^3 in (2.2) needs to be considered and all the other curvature related terms in (2.1)–(2.3) are of higher order and can be neglected. In a channel geometry, it can be shown that this term produces the well-known Dean number and the effects of Reynolds number Re and curvature can be described by a single Dean number (cf. Drazin & Reid 1981). For a concave boundary layer with $\partial \bar{p}^0/\partial\theta = 0$, it can be shown (rather straightforwardly) that this term produces the Görtler number, and (2.1)–(2.3) are then identical to those in Hall (1988, equation 2.4), which have been shown to be correct to order $Re^{-\frac{1}{2}}$.

(*b*) When R is finite ($\gamma < 0.99$), it has been shown in the case of the Dean problem (cf. Finlay *et al.* 1988) that the other high-order curvature terms will affect the stability boundary significantly, and the retaining of these terms in (2.1)–(2.3) is essential. In this study, γ is chosen to be 0.975 in the case of the Dean problem. In the Görtler problem, the effects of finite R have never been addressed before and in this study $\gamma > 0.995$. For completeness, we keep all curvature-induced terms in (2.1)–(2.3) in this study.

(*c*) Equations (2.1)–(2.3) can also be derived from the frame of the parabolized stability equations (PSE) proposed by Bertolotti *et al.* (1992). When periodic boundary conditions are used in the spanwise direction, the flow $\boldsymbol{u}^0$ can be written as

$$\boldsymbol{u}^0 = \sum_{n=-\infty}^{\infty} \tilde{\boldsymbol{u}}_n^0(r, \theta) \exp(n\alpha z), \tag{2.4}$$

where α is the spanwise wavenumber of $\boldsymbol{u}^0$. There are only spanwise wavenumbers in the above expansion and the streamwise wavenumbers of the flow can be considered to be zero. Substituting the above expansion into the nonlinear PSE, one can arrive at (2.1)–(2.3) naturally. So in this sense, (2.1)–(2.3) are a special case of PSE.

2.2. *Spatial Eckhaus instability*

Once the developing Dean and Görtler vortices $\boldsymbol{u}^0$ are found from (2.1)–(2.3), the stability of $\boldsymbol{u}^0$ with respect to spanwise perturbation can be studied by substituting

$$\boldsymbol{u} = \boldsymbol{u}^0 + \boldsymbol{u}' \tag{2.5}$$

into the Navier–Stokes equations. Here, $\boldsymbol{u}'$ is a perturbation of the form (cf. Guo & Finlay 1991)

$$\boldsymbol{u}' = \tilde{\boldsymbol{u}}(r, \theta, z) \exp(\mathrm{i}\beta z), \tag{2.6}$$

where β is the perturbation wavenumber and $\tilde{\boldsymbol{u}}$ is the complex eigenfunction, which can be written as

$$\tilde{\boldsymbol{u}} = \sum_{n=-\infty}^{\infty} \tilde{\boldsymbol{u}}_n(r, \theta) \exp(in\alpha z), \tag{2.7}$$

where α is the wavenumber of the base flow $\boldsymbol{u}^0$. In some cases it is more convenient to

use the non-dimensionalized wavenumber $b = \beta/\alpha$. The flow pattern of the perturbation is given by the real part of (2.6). Note that $\tilde{\boldsymbol{u}}$ is a function of θ and is not normalized. The spatial growth rate of $\boldsymbol{u}'$ can be calculated from $\tilde{\boldsymbol{u}}$ (ref. equation 2.14). Physically, the instability defined by (2.6) represents the interactions that occur between developing Dean or Görtler vortices. In most experimental observations and numerical simulations, Dean or Görtler vortices with a well-defined wavenumber are seen at a specific location. One myth is that the development of one wavenumber suppresses the growth of other wavenumbers so that only one wavenumber is observed at one location. To resolve this issue is one of the motivations for carrying out this study.

It can be shown that the perturbation of the form (2.6) is contained in (2.1)–(2.3). For example, the perturbation with $b = 0.5$ can be calculated from (2.1)–(2.3) by including two pairs of vortices in the computational box. But in practice this is inconvenient and also expensive sometimes. For example, $b = 0.1$ means ten pairs of vortices must be included in the box in order to calculate the corresponding perturbation. Besides, nonlinear interactions among different spanwise modes of the base flow also make such an approach rather inaccurate. In this paper, this instability is studied by the linear 'parabolized' stability equations derived by substituting (2.6) into the Navier–Stokes equations and applying a parabolization approach identical to that of (2.1)–(2.3). For simplicity, we use Cartesian coordinates to illustrate our formulation. With the streamwise direction x and spanwise direction z, the stability equations can be written in the streamwise direction as

$$2\frac{\partial}{\partial x}(u_x^0\,\tilde{u}_x) + w_x = \frac{1}{Re}\left[\frac{\partial^2\tilde{u}_x}{\partial y^2} + \frac{\partial^2\tilde{u}_x}{\partial z^2}\right] \tag{2.8}$$

and in the cross-stream directions as

$$\frac{\partial}{\partial x}(u_x^0\,\tilde{u}_y) + \frac{\partial}{\partial x}(u_y^0\,\tilde{u}_x) + w_y = -\frac{\partial\tilde{p}}{\partial y} + \frac{1}{Re}\left[\frac{\partial^2\tilde{u}_y}{\partial y^2} + \frac{\partial^2\tilde{u}_y}{\partial z^2}\right], \tag{2.9a}$$

$$\frac{\partial}{\partial x}(u_x^0\,\tilde{u}_z) + \frac{\partial}{\partial x}(u_z^0\,\tilde{u}_x) + w_z = -\frac{\partial\tilde{p}}{\partial z} - \mathrm{i}\beta\tilde{p} + \frac{1}{Re}\left[\frac{\partial^2\tilde{u}_z}{\partial y^2} + \frac{\partial^2\tilde{u}_z}{\partial z^2}\right]. \tag{2.9b}$$

The continuity equation is

$$-\frac{\partial\tilde{u}_y}{\partial y} - \left(\frac{\partial}{\partial z} + \mathrm{i}\beta\right)\tilde{u}_z = \frac{\partial\tilde{u}_x}{\partial x}, \tag{2.10}$$

where $w_k = \dfrac{\partial}{\partial y}(u_y^0\,\tilde{u}_k + \tilde{u}_y\,u_k^0) + \left(\dfrac{\partial}{\partial z} + \mathrm{i}\beta\right)(u_z^0\,\tilde{u}_k + \tilde{u}_z\,u_k^0) - \dfrac{1}{Re}\left(2\mathrm{i}\beta\dfrac{\partial\tilde{u}_k}{\partial z} - \beta^2\tilde{u}_k\right) + f_k.$

Here $k = x$, y and z and f_k result from nonlinear curvature terms. The base flow $\boldsymbol{u}^0$ in (2.8)–(2.10) is provided by (2.1)–(2.3). The absence of pressure in the streamwise moment equation (2.8) is because the perturbation pressure of the form (2.6) is zero when averaged on the cross-stream plane. Since (2.6) is a subset of the solution of (2.1)–(2.3), the parabolization process used to derive (2.8)–(2.10) can be justified in the same fashion as for (2.1)–(2.3).

2.3. *Some comments on equations* (2.1)–(2.3) *and* (2.8)–(2.10)

Theoretically, equations (2.1)–(2.3) should be solved first to obtain the base flow $\boldsymbol{u}^0$. Then the stability equations (2.8)–(2.10) can be solved using the stored base flow data. Since both sets (2.1)–(2.3) and (2.8)–(2.10) have a parabolic nature in the streamwise

direction, only the inflow boundary conditions at θ_0 (or x_0) are needed. Their solutions can be marched downstream simultaneously, with the solution of (2.1)–(2.3) being one step ahead of that of (2.8)–(2.10). There is no need to store the base flow data.

In order to trigger the development of nonlinear Dean or Görtler vortices in the base flow, small (linear) disturbances are usually introduced in the initial flow condition (i.e. inflow condition) at $\theta = \theta_0$ to start the calculation of (2.1)–(2.3). For channel flows, θ_0 is irrelevant and we set $\theta_0 = 0$. For boundary-layer flows, $x_0 = \theta_0 R$ is meaningful. The solution of the stability equations (2.8)–(2.10) is also marched downstream with certain initial eigenfunctions at the same θ_0 as that of the base flow.

Concerning the nature of the stability equations (2.8)–(2.10), we have the following comments. When the base flow is set to be one-dimensional Poiseuille flow, (2.8)–(2.10) contain the spatial Dean instability studied by Matsson & Alfredsson (1990). When the base flow is set to be Blasius flow, (2.8)–(2.10) reduce to those of Hall (1983) in the limit of $Re \to \infty$ and $R \to \infty$, which have been shown to govern Görtler instability correctly to order $Re^{-\frac{1}{2}}$. When the base flow develops from Poiseuille flow or Blasius flow into nonlinear Dean or Görtler vortices, the character of (2.8)–(2.10) changes from Dean or Görtler instability to the instability of these nonlinear vortices with respect to spanwise perturbation, i.e. spatial Eckhaus instability. This instability sets in only when the vortices in the base flow become nonlinear and thus is different from primary instability (Dean or Görtler instability).

Once the most unstable wavenumber β is found from (2.8)–(2.10), the nonlinear development of this perturbation can be studied by (2.1)–(2.3) with a computational box which can hold m pairs of base vortices. Here m is the minimum number that makes $m \times \beta/\alpha$ an integer. Our results show that the most unstable wavenumber for spatial Eckhaus instability in this study is usually $\frac{1}{2}\alpha$ or $\frac{3}{2}\alpha$. So only two pairs of vortices need to be included in a computational box in order to study the nonlinear dynamics of this instability.

2.4. *A Legendre spectral-element method*

Control-volume methods (Patankar & Spalding 1972), finite-difference methods (Rubin, Khosla & Saari 1977) and finite-element methods (Baker 1983) have been used to solve (2.1)–(2.3). In this study, we choose a Legendre spectral-element method (Rønquist 1988; Maday & Patera 1989). The combination of the high accuracy of spectral methods with the geometry flexibility of finite-element methods make the spectral-element methods particularly suitable for this study. For example, to switch from Dean vortices to Görtler vorties, we only need to modify the boundary conditions, which requires only minor code changes. This advantage helps us to verify the numerical codes developed in this study and gives us confidence in our results for the Görtler problem. Boundary layers can also be captured easily by using small elements near the wall. Thus there is no need to use a coordinate transformation.

In the streamwise direction, a third-order Adam–Bashforth (AB3) scheme is used for the nonlinear convection terms and curvature terms, while a backward Euler scheme is used for the viscous terms. This combination is motivated by the fact that the spatial marching step size is mostly limited by the explicit treatment of the nonlinear terms in (2.1)–(2.3) and a third-order Adam–Bashforth scheme offers a reasonably large numerical stability region. We have also tried a Crank–Nicolson scheme for the viscous terms, but since our numerical experiments found no significant difference in accuracy or numerical stability, this scheme is not used in this study.

Though (2.1)–(2.3) are different from any example given by Rønquist (1988) and Maday & Patera (1989), following the procedures they give and standard variational principles, the discretization of (2.1)–(2.3) in an (r, z)-plane is straightforward. Within

each element, the velocity $\boldsymbol{u}^0$ is represented on $(N+1)(N+1)$ Gauss–Lobatto/Gauss–Lobatto Legendre nodes by Legendre–Lagrange interpolating polynomials of degree N. The pressure p^0 is represented on $(N-1)(N-1)$ Gauss/Gauss Legendre nodes by Legendre–Lagrange interpolating polynomials of degree $(N-2)$. The resulting matrix system can be written in the streamwise direction as

$$2B_\theta^n \frac{U_\theta^{n+1}-U_\theta^n}{\Delta\theta}+\sum_{l=0}^{2}\beta_l(C_\theta-F_\theta)^{n-l}=-B\bar{P}_\theta^{n+1}-\frac{1}{Re}AU_\theta^{n+1}, \tag{2.11}$$

and in the cross-stream directions as

$$\frac{B_\theta^{n+1}U_i^{n+1}-B_\theta^n U_i^n}{\Delta\theta}+\sum_{l=0}^{2}\beta_l(C_i-F_i)^{n-l}=D_i P^{n+1}-\frac{1}{Re}AU_i^{n+1}. \tag{2.12}$$

The continuity equation is

$$-D_r^T U_r^{n+1}-D_z^T U_z^{n+1}=\frac{B_p^T}{\Delta\theta}(U_\theta^{n+1}-U_\theta^n). \tag{2.13}$$

Equation (2.12) contains two equations, obtained by setting $i=r$ and z. The symbol U_i^n is the vector consisting of ϕ_i at the Gauss–Lobatto/Gauss–Lobatto nodes at step n; $\bar{P}_\theta^{n+1}$ is the streamwise pressure gradient averaged across the (r,z)-plane at step $n+1$; P^{n+1} is the vector consisting of the pressure p at the Gauss/Gauss nodes at step $n+1$. The symbols A, B and D_i are the standard Laplace matrix, mass matrix (lumped) and gradient matrices; B_θ^n is the lumped mass matrix of ϕ_θ/r^3 on the Gauss–Lobatto/Gauss–Lobatto nodes at step n, and B_p is the mass matrix on the Gauss/Gauss–Lobatto nodes. C_i and $F_i(i=r,\theta,z)$ are from the convection and curvature terms. The coefficient $\beta_l=\frac{23}{12}$, $-\frac{16}{12}$ and $\frac{5}{12}$ for $l=0$, 1 and 2 respectively. More details regarding the discretization of (2.1)–(2.3) can be found in Guo (1992).

The following strategies are used to march the solutions of (2.1)–(2.13) in the streamwise direction. The streamwise momentum equation (2.11) is marched first from step n to step $n+1$ to give U_θ^{n+1}; B_θ^{n+1} is then calculated from U_θ^{n+1}. For the flow on a concave wall, $\bar{P}_\theta^{n+1}$ is set to zero. For channel flow, $\bar{P}_\theta^{n+1}$ is found by forcing the flow rate

$$Q=\int u_\theta^{n+1}\,\mathrm{d}r\,\mathrm{d}z$$

to be constant. This is done by a steepest-descent iterative method. Once U_θ^{n+1} and B_θ^{n+1} are known, P^{n+1}, U_r^{n+1} and U_z^{n+1} can be solved for the cross-stream momentum equations (2.12) and the continuity equation (2.13) using a global iterative Uzawa scheme similar to the one used by Rønquist (1988). Because $u_\theta=0$ at walls, the popular pressure Poisson equation decoupling approaches (for example Patera 1984; Kleiser & Schumann 1984) are not applicable for (2.2) and (2.3) (the derived Poisson equation for pressure is singular at walls). Preconditioned conjugate iterative methods similar to those used by Rønquist (1988) are used to deal with the resulting linear matrix problems.

The discretization of the stability equations (2.8)–(2.10) follows that of (2.1)–(2.3). The solutions of (2.8)–(2.10) are marched in the streamwise direction together with (2.1)–(2.3) using a strategy similar to that for (2.11)–(2.13). More details can be found in Guo (1992).

Once the perturbation $\boldsymbol{u}'$ is found, the energy growth rate σ of the perturbation can be calculated from

$$\sigma=(\ln \mathrm{e}^{n+1}-\ln \mathrm{e}^n)\frac{l}{2\Delta x}, \tag{2.14}$$

where e is the energy of the perturbation defined by

$$e = \int |\boldsymbol{u}|^2 \, \mathrm{d}r \, \mathrm{d}z,$$

and l is the lengthscale used to non-dimensionalize σ. For Dean vortices, the channel half-width, $\frac{1}{2}d$, is used for l. For Görtler vortices, the streamwise distance x from the leading edge is used. In cylindrical coordinates, $\Delta x = \Delta\theta \frac{1}{2}(r_o - r_i)$ for channel flows and $\Delta x = R\Delta\theta$ for growing boundary layers. In some cases, the growth rate σ_1 defined by

$$\sigma_1 = (\ln |u_\theta'^{n+1}|_{max} - \ln |u_\theta'^{n}|_{max}) \frac{l}{\Delta x}$$

is also used. For the linear stability equations (2.8)–(2.10), the absolute energy level of the perturbation $\boldsymbol{u}'$ is irrelevant.

In this study, the orders of the polynomials used for each spectral element are 8, 10, or 12. For the simulation and stability analysis of Dean vorties, usually 2–4 elements are used in the radial directions, depending on *Re*. For the simulation and stability analysis of Görtler vortices, the number of elements in the radial direction varies from 3 to 6. The computational grid extends to at least $8\delta_{0.99}$ normal to the wall. In the spanwise direction, the number of elements depends on the aspect ratio of the computational box. The minimum is two.

3. Code verification

Since the numerical schemes we use to solve the parabolized Navier–Stokes equations (2.1)–(2.3) and the related stability equations (2.8)–(2.10) have never been reported before, proper code verifications are crucial. In the rest of this study, we will refer to the code that solves (2.1)–(2.3) as the 'simulation code' and the code that deals with (2.8)–(2.10) as the 'stability code'.

3.1. *Verification of the simulation code*

For fully developed channel flow, our simulation code can accurately duplicate the velocity and pressure of the fully developed nonlinear Dean vortices given by Finlay *et al.* (1988) and Guo & Finlay (1991), regardless of what initial conditions are used to start the simulations. The simulations of developing Dean vortices cannot be verified directly because the velocity and pressure of the developing Dean vortices depend both on the initial conditions and the streamwise location and there are no such data available. However, through the manipulation of initial flow conditions, our numerical results can be made to match the data given by Matsson & Alfredsson (1992) experimentally and by Bottaro, Matsson & Alfredsson (1991) numerically. Another indirect verification is given by the fact that the streamwise growth of developing Dean vortices from the simulation code is accurately predicted by the stability code, i.e. both our codes gives the same growth rates for linear Dean vortices (see § 5). Since these two codes use different theories and formulations, it is unlikely that both codes have errors that lead to the same results.

In the geometry of a flat plate, the code can accurately duplicate the Blasius velocity profile (Schlichting 1955). On a concave surface, through the manipulation of the energy level of the perturbtions near the leading edge, Görtler vortices with strength comparable with those observed by Swearingen & Blackwelder (1987) and Lee & Liu

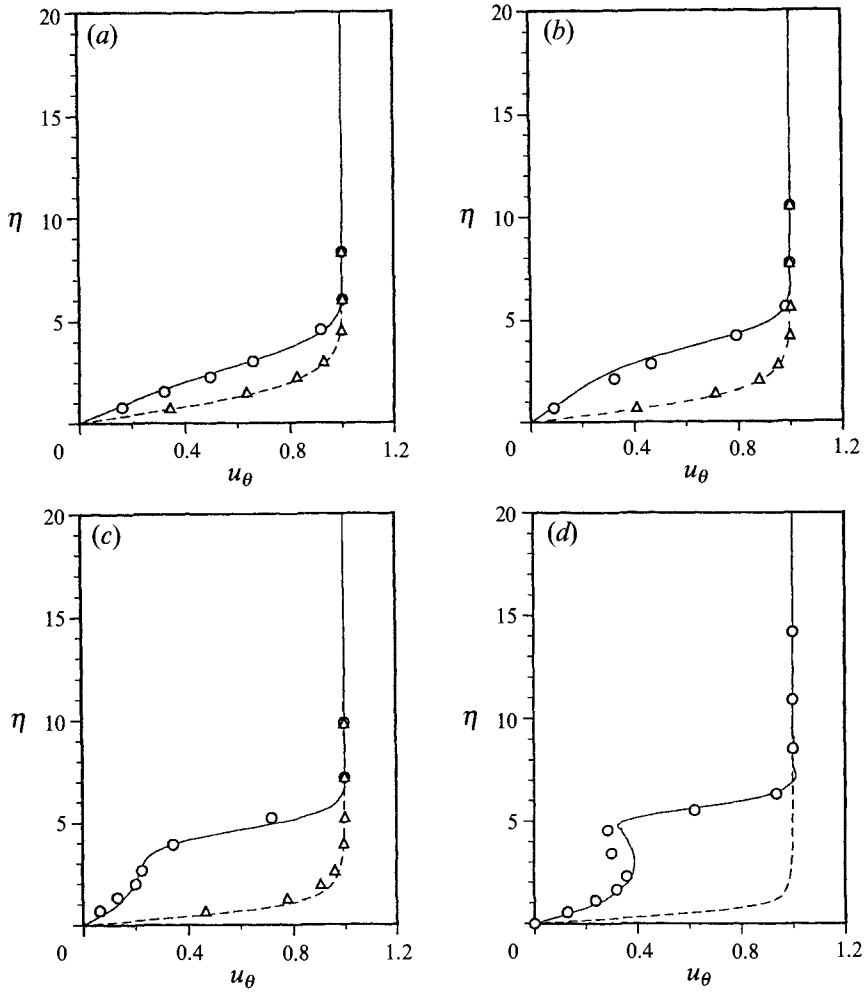

FIGURE 3. Velocity profile u_θ at the peak (——) and valley (– – –) of Görtler vortices with $\lambda = 1.8$ cm is shown as a function of $\eta = y(U_\infty/\nu x)^{\frac{1}{2}}$ at (*a*) $x = 60$ cm; (*b*) $x = 70$ cm; (*c*) $x = 80$ cm and (*d*) $x = 90$ cm. The data of Swearingen & Blackwelder (1987) are given as ○ (peak) and △ (valley).

(1992) can also be produced by our simulation code. Figure 3 shows a comparison of the streamwise velocity u_θ at different x with the data from Swearingen & Blackwelder (1987). The spanwise wavelength $\lambda = 1.8$ cm on a concave wall with radius $R = 3.2$ m. The free-stream velocity U_∞ is 5 m s^{-1} and the kinematic viscosity ν is 14.5×10^{-6} m s^{-2}. The simulation is started at a distance $x = 12.8$ cm from the leading edge using the initial flow condition $\boldsymbol{u}^0 = (0.4 v_B \sin(2\pi z/\lambda), u_B, 0)$; v_B and u_B are the vertical and streamwise components of Blasius boundary-layer flow. Different initial conditions can also give Görtler vortices of the same strength. It can be seen that the agreement is good up to $x = 90$ cm. For $x \geqslant 100$ cm in Swearingen & Blackwelder (1987), Görtler vortices begin to develop into time-dependent wavy vortices and horseshoe-type vortices and they break down shortly afterwards.

Sabry & Liu (1991) and Lee & Liu (1992) give a similar comparison with the experimental observations of Swearingen & Blackwelder (1987) using a temporal theory and spatial parabolized methods. In general, their results from temporally and spatially evolving Görtler vortices are quite similar to ours. Readers are referred to

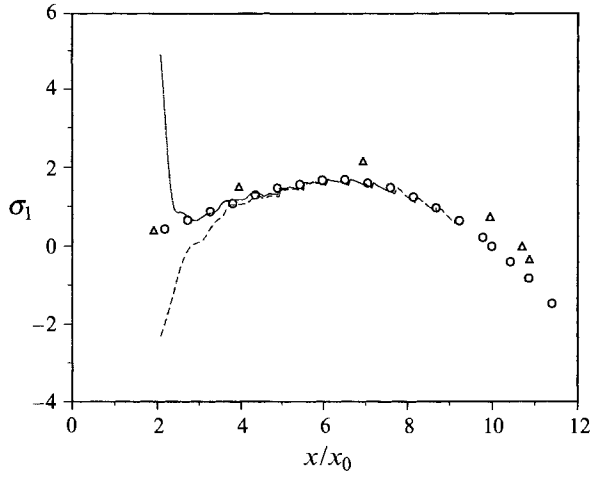

FIGURE 4. The growth rates σ_1 of linear Görtler vortices with $\Lambda = 62$ are shown as functions of streamwise distance from the leading edge x/x_0, where x_0 is the streamwise location of the neutral point given by a local method. The values of σ_1 (– – –) are obtained with the initial eigenfunctions $(-v_B, 0, 0)$; the σ_1 (——) are obtained with the initial eigenfunctions $(0, u_B, 0)$, where u_B and v_B are the streamwise and vertical components of Blasius flow. The growth rates σ_1 obtained by Day *et al.* (1990) using a local method (△) and a global marching method (○) are also given.

Sabry & Liu (1991) and Lee & Liu (1992) for more details on the nonlinear features of Görtler vortices, since this is not the topic of this study.

3.2. *Verification of the stability code*

In the channel geometry, the stability code can accurately duplicate the primary instability boundary from a temporal theory (Guo & Finlay 1991) by setting the base flow $\boldsymbol{u}_0$ in (2.8)–(2.10) to be one-dimensional Poiseuille flow. The growth rates given by the spatial stability code are the same as those given by our simulation code. We can also accurately duplicate the results given by Matsson & Alfredsson (1990) for the primary spatial instability associated with Dean vortices.

When the base flow is set to be fully developed Dean vortices, the stability code can accurately duplicate the stability boundary of Eckhaus instability given by Guo & Finlay (1991) using temporal theory. The code also gives growth rates and eigenfunctions which are symmetric in b about $b = \beta/\alpha = 0.5$, and have the following property:

$$f(b) = f(b \pm n). \tag{3.1}$$

Here $f(b)$ represents the spatial growth rate and eigenfunction at b, and $n = 1, 2, 3, \ldots$. Since (3.1) can be derived analytically for any spanwise periodic flow (Guo & Finlay 1991; Guo 1992), we believe that our stability code is working properly for fully developed flows.

For spatially developing flow, the stability code can be verified by the linear stability analysis of Görtler vortices. When the base flow $\boldsymbol{u}^0$ in (2.8)–(2.10) is set to be Blasius flow, the stability code is equivalent to the global marching method used by Hall (1983). First, our code confirms Hall's results that the stability boundary depends very much on how and where the initial perturbations are used to start the analysis. Further downstream, our results confirm the statement in Hall (1983) that the growth rates converge to a unique curve which does not depend on the initial perturbations.

Figure 4 shows the typical development of the growth rates for Görtler vortices with the wavelength parameter $\Lambda = 62$. Also given for comparison are the growth rates

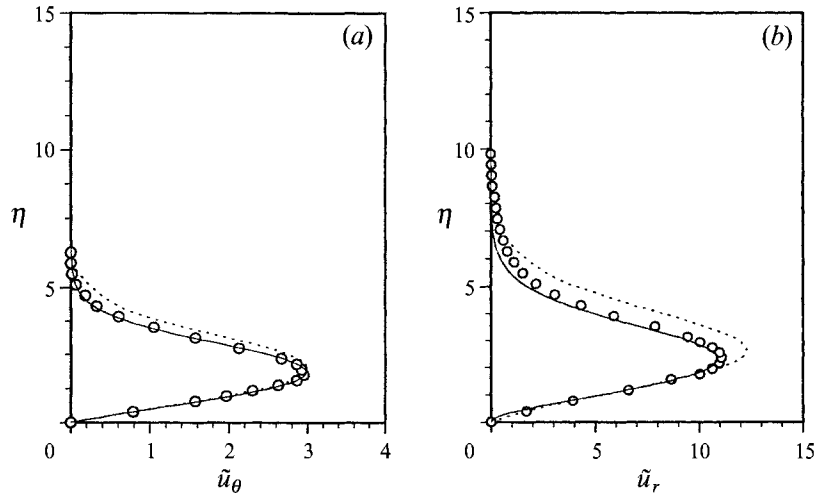

FIGURE 5. Comparison of the eigenfunction components (*a*) $\tilde{u}_\theta$ and (*b*) $\tilde{u}_r$ of linear Görtler vortices (——) with the data obtained by Day *et al.* (1990) using a local method (.....) and a global marching method (○). Distance from the wall is $\eta = y(U_\infty/\nu x)^{\frac{1}{2}}$ and $\tilde{u}_r$ is scaled by $U_\infty x_0/\nu$.

calculated by Day *et al.* (1990) using a local approach (Floryan & Saric 1984) and a global marching method (Hall 1983). In figure 4, x_0 is the streamwise location of the neutral point given by the local method. For $\Lambda = 62$, the neutral Görtler number from the local method is $G_0 = 0.998$. It can be seen that our neutral points depend on the initial perturbations and locations used to start the marching. The difference between the data given by Day *et al.* and ours for $x/x_0 < 4.0$ is due to the different initial perturbations used to start the marching. Day *et al.* use the eigenfunctions for local theory as the initial perturbations. The fluctuations in the growth rate σ_1 of $|u'_\theta|_{max}$ are associated with unevenly spaced grid points in the r used by spectral-element methods. Since the integration of $|\boldsymbol{u}'|^2$ over the cross-stream plane is less affected by this factor, we will use only the energy growth rate σ in the rest of this paper.

A comparison of the perturbation velocity profiles is given in figure 5 for $\Lambda = 62$ at $x/x_0 = 4$. Again the agreement is reasonable. In figure 5(*b*), u'_r is scaled by $U_\infty x_0/\nu$ (a factor of 1200). The small discrepancies in figure 5(*b*) are likely caused by the inaccuracy in measuring x_0 (we calculated it from G_0 given by Day *et al.*) and the higher-order curvature terms kept in (2.8)–(2.10).

4. Eckhaus instability of spatially developing Dean and Görtler vortices

In this section, we first present four case studies of Dean and Görtler vortices with small and large wavenumbers, and then discuss some general features of spatial Eckhaus instability. For Dean vortices, the case studies are presented at $Re = 2.0Re_c$ in a curved channel with $\gamma = 0.975$. The initial flow condition used to start the simulation code is $\boldsymbol{u}^0 = (0, u_{1D}(1.0 + \sin(2\pi\alpha z) \times 10^{-4}), 0)$, where u_{1D} is the velocity of curved channel Poiseuille flow. The field $(0, u_{1D}, 0)$ is used as the real part of the initial eigenfunction to start the stability code (the imaginary part is zero). We have tried different forms of initial eigenfunctions and found no difference in the growth rate and perturbation pattern.

In the Görtler problem, we use a concave wall with radius $R = 3.2\,\text{m}$, free-stream velocity $U_\infty = 5\ \text{m s}^{-1}$ and kinematic viscosity $\nu = 14.5 \times 10^{-6}\ \text{m s}^{-2}$. These parameters

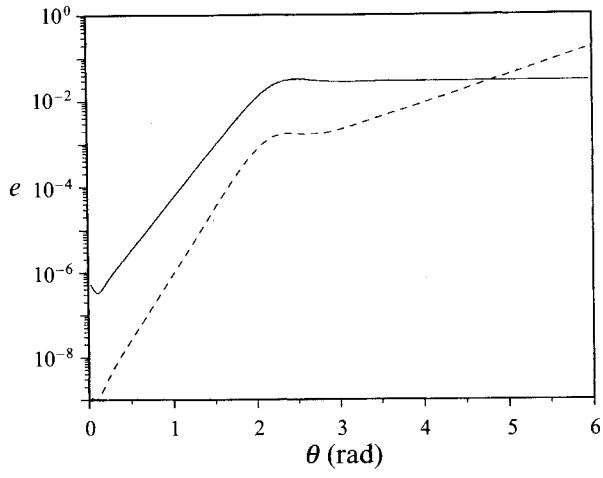

FIGURE 6. Spatial growth of the energies of the base Dean vortices $\alpha = 4.0$ (——) and the related perturbation $\beta = 2.0$ ($b = 0.5$) of spatial Eckhaus instability (– – –).

are also used by Swearingen & Blackwelder (1987). The initial flow condition used for the base flow $\boldsymbol{u}^0$ is

$$\boldsymbol{u}^0 = (\epsilon v_B \cos(2\pi z/\lambda), u_B, 0), \tag{4.1}$$

where u_B and v_B are the streamwise and vertical velocities of Blasius flow and ϵ is used to adjust the initial energy level of the disturbances in the base flow. The initial eigenfunction

$$\tilde{\boldsymbol{u}} = (-v_B, 0, 0) \tag{4.2}$$

is used for both the real and imaginary parts of the related eigenfunctioins of Eckhaus instability.

4.1. *Dean vortices with large wavenumber*

Figure 6 shows the development of the energy of the perturbation defined by (2.6). Also given for reference is the energy of Dean vortices in the base flow. Note that the absolute energy level of the perturbation in (2.8)–(2.10) is irrelevant. The wavenumber of the base Dean vorties is $\alpha = 4.0$. The perturbation wavenumber is $\beta = 2.0$ ($b = 0.5$). When $\theta < 1.5$, the growth rates of the base Dean vortices and the related perturbation are 0.071 and 0.09, which are equal to the growth rates of primary instability at $\alpha = 4.0$ and 2.0. This indicates that when the Dean vortices in the base flow have small amplitude, the growth of each wavenumber is governed by primary instability. Different wavenumbers do not interact with each other at this stage. This is to be expected and can be shown analytically.

The growth rate of the perturbation remains near 0.09 until $\theta = 1.75$, where the base Dean vortices have reached a significantly nonlinear level. When the base Dean vortices are fully developed at $\theta = 3.0$, the growth rate of the perturbation changes to 0.019. This value is very close to the one given by the spatial Eckhaus instability using the fully developed Dean vortices $\alpha = 4.0$ as the base flow. Thus the energy of the perturbation with $b = 0.5$, which grew initially due to a primary instability, is transferred into an Eckhaus instability once the base vortices become strongly nonlinear (at $\theta > 2.5$ or so). In figure 6 we can also see that the energy of the perturbation continues to grow while the base Dean vortices are developing.

Figure 7 shows the spatial development of the radial velocity component of the base

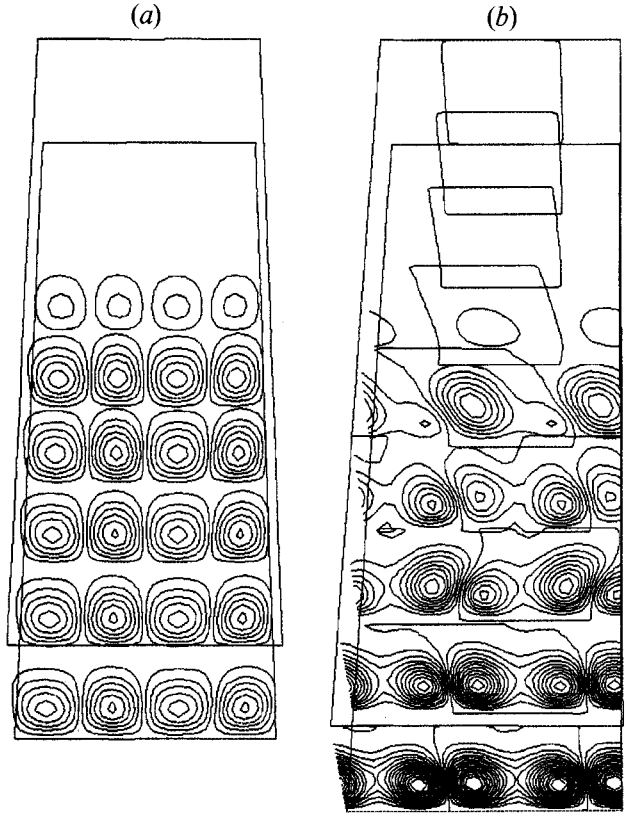

FIGURE 7. Contours of the velocity components (*a*) u_r^0 of the base Dean vortices and (*b*) u_r' of the related perturbation in figure 6 are shown in cross-stream planes from the streamwise location $\theta = 0.26$ to 4.26 rad with $\Delta\theta = 0.5$ rad. The inner wall is above the outer wall and the flow proceeds downstream from top to bottom. Contours: (*a*) $-0.065 : 0.055$ with contour increment 0.01. (*b*) $-0.7 \times 10^{-3} : 0.7 \times 10^{-3}$ with contour increment 0.5×10^{-4}.

flow and the perturbation in figure 6. In figure 7(*a*), the base Dean vortices become visible at $\theta = 1.76$. There are two vortex pairs shown in the domain because $b = 0.5$. When $\theta > 2.5$, the base vortices become fully developed. In figure 7(*b*), it can be seen that though there is always one pair of vortices in the perturbation, the shape of the perturbation begins to change at $\theta = 1.76$, where the base flow develops into nonlinear Dean vortices. From $\theta = 1.76$ to 3.0, the perturbation pattern experiences a spanwise shift. The increased density of the contour lines also indicates an increase of energy in the perturbation. By $\theta = 3.76$, the shape of the perturbation stops changing.

The flow patterns of the base flow and the perturbation at $\theta = 4.26$ are shown in figure 8(*a*) and 8(*b*) in the cross-stream plane. The velocities in figure 8 (and all other vector plots in the rest of the paper) are shown on the grid points actually used in the computation. In figure 8(*a*), there are two pairs of nonlinear Dean vortices in the domain. The related perturbation in figure 8(*b*) has only one pair of vortices in the space of two base pairs. Its shape is quite similar to those given by Guo & Finlay (1991) using a temporal theory. In Guo & Finlay, the effect of this type of perturbation on the base flow is demonstrated by superimposing the perturbation on the base flow. Following the same procedure, we find an identical situation: the two base vortices near $2z/d = 1.6$ and 2.4 in figure 8(*a*) are being forced together and become smaller. These two vortices are separated by an outflow region where the fluid flows from the

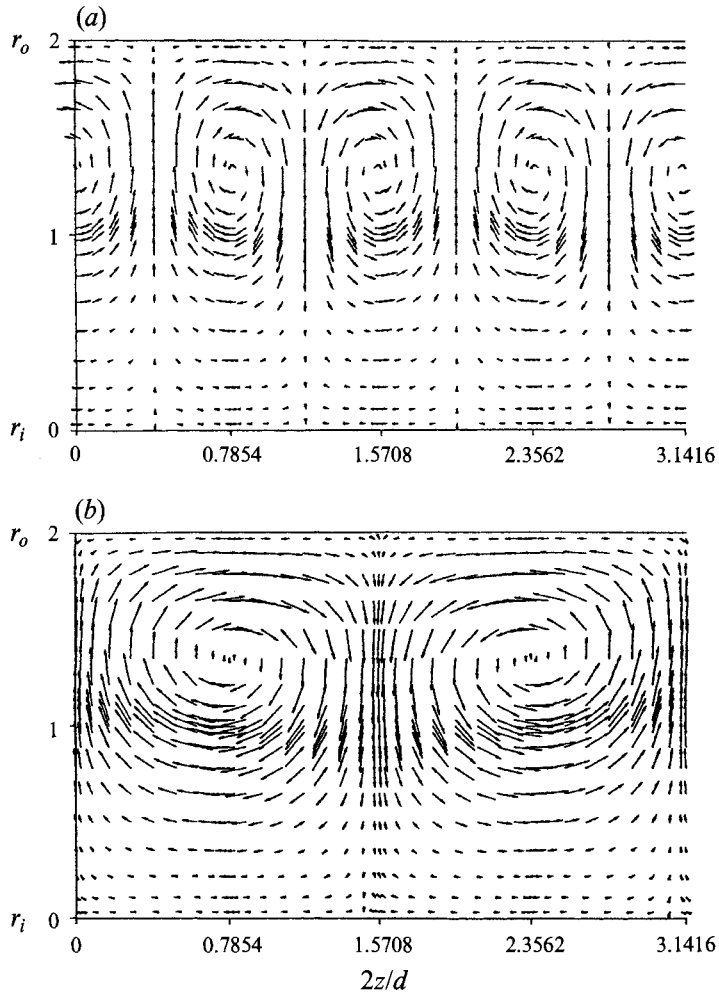

FIGURE 8. Base Dean vortices (*a*) and the related perturbation (*b*) in figure 7 are projected onto the (r, z)-plane at $\theta = 4.26$.

convex (inner) wall to the concave (outer) wall. In the context of temporal theory, the nonlinear development of this type of perturbation is found to lead to the merging of two vortex pairs into one pair (Guo & Finlay 1991).

4.2. *Görtler vortices with short wavelength*

Figure 9 shows the development of the energy of the base Görtler vortices with $\lambda = 0.749$ cm ($\Lambda = 125$) and the related perturbation of spatial Eckhaus instability with $\lambda_1 = 1.498$ cm ($b = 0.5$). Also given are the energies of linear Görtler vortices from primary instability at $\lambda = 0.749$ cm and 1.498 cm. Both the simulation code and the stability code are started at $x = 9.6$ cm with $\epsilon = 0.1$ in equation (4.1).

It can be seen that the growth of the base Görtler vortices is well predicted by primary instability for $0.35 < x < 0.6$ m, where the base vortices are linear. When $x > 0.6$ m, where the nonlinearity of the base Görtler vortices sets in, the growth of the perturbation begins to change and the spatial Eckhaus instability becomes visible. As in the case of developing Dean vortices, the growth rate of the perturbation is always positive.

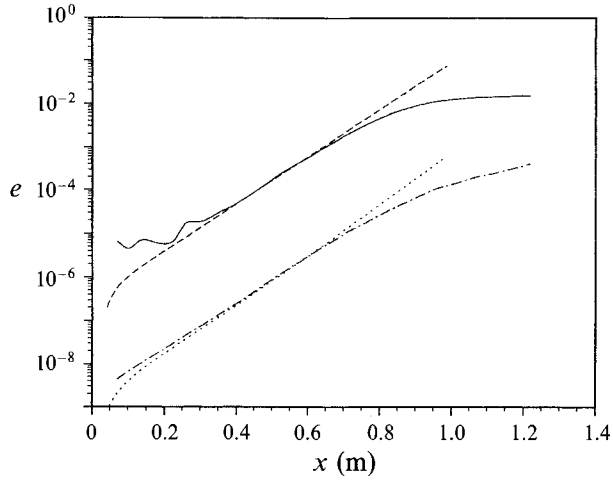

FIGURE 9. Energies of the base Görtler vortices $\lambda = 0.749$ cm ($\Lambda = 125$, ——) and the related perturbation $\lambda_1 = 1.498$ cm ($b = 0.5$) of spatial Eckhaus instability (—·—). The energies of linear Görtler vortices from primary instability with $\lambda = 0.749$ cm (– – –) and 1.498 cm (.....) are also given.

In figure 9, the discrepancies for $x < 0.35$ m are partly due to the fact that the disturbance used to start the simulation is not the most unstable solution of the parabolized Navier–Stokes equations. In general cases, although different initial conditions lead to different solutions, the most unstable eigensolutions will grow out of the transient solution associated with a given initial condition and dominate the solution downstream, while the other components of the transient solution will decay. So a certain distance downstream, these eigensolutions will converge to a unique solution (cf. figure 4 in this study, Hall 1983 and Day *et al.* 1990). Since the instability of interest in this study sets in only when the solutions are marched downstream a certain distance where the base vortices become nonlinear, the arbitrariness in initial conditions used for the base flow and perturbation do not affect our results.

Figure 10 shows the cross-stream flow patterns of both base flow and perturbation at $x = 1.169$ m where the base vortices are nonlinear. In figure 10(*b*), one can see that on top of the two vortices near the wall there are another two vortices, far away from the wall. In the spanwise direction, there is only one pair of vortices in the domain, compared to two pairs of the base flow in figure 10(*a*). This is different from the Dean vortices in figure 8(*b*). To demonstrate the effect of the perturbation on the base flow, the perturbation in figure 10(*b*) is superimposed on the base vortices in figure 10(*a*) and is shown in figure 10(*c*). The amplitude of the perturbation is 16.7% of the base flow's amplitude (which is not a linear perturbation but the large perturbation is used for visual clarity). For the base vortex pair with an outflow region at $z/\lambda = 1.0$ in figure 10(*a*), the lower half of the vortex pair near the wall is squeezed together by the two perturbation vortices near the wall in figure 10(*b*), so that its dimension in the spanwise direction becomes less. The upper half of this vortex pair is amplified by the two perturbation vortices away from the wall, and as a result it becomes elongated in the radial direction and grows bigger. For the base vortex pair near $z/\lambda = 0$ (or 2.0) in figure 10(*a*), the lower half of the vortex pair near the wall is enhanced by the two perturbation vortices near the wall (figure 10*b*) and grows stronger, while its upper half is weakened by the two perturbation vortices away from the wall. As a result, this vortex pair moves closer to the wall. If this character of the perturbation is maintained

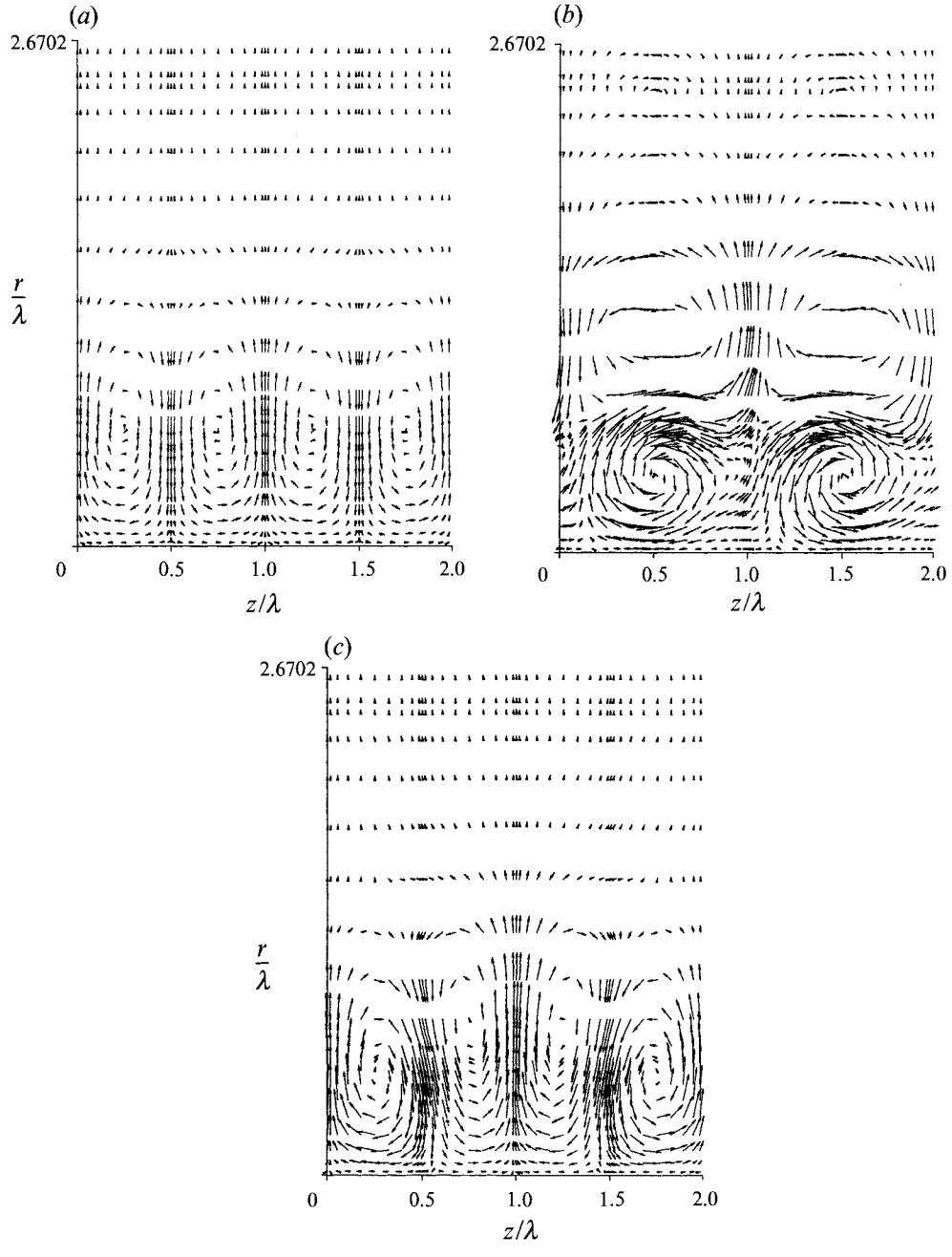

FIGURE 10. Base Görtler vortices and the perturbation of figure 9, are projected onto the (r, z)-plane at $x = 1.169$ m (in *a* and *b*); (*c*) shows (*a*) $+16.7\%$ of (*b*).

in the nonlinear state, we can expect that the vortex pair centred near $z/\lambda = 1.0$ will be ejected from the wall, to be replaced by the other two vortices. The nonlinear aspect of this development will be studied in §5.3.

Unlike the Dean problem, the perturbation pattern of spatial Eckhaus instability for Görtler vortices is sensitive to the spanwise phase difference between the base vortices and the perturbation before the onset of the Eckhaus instability. Our numerical results

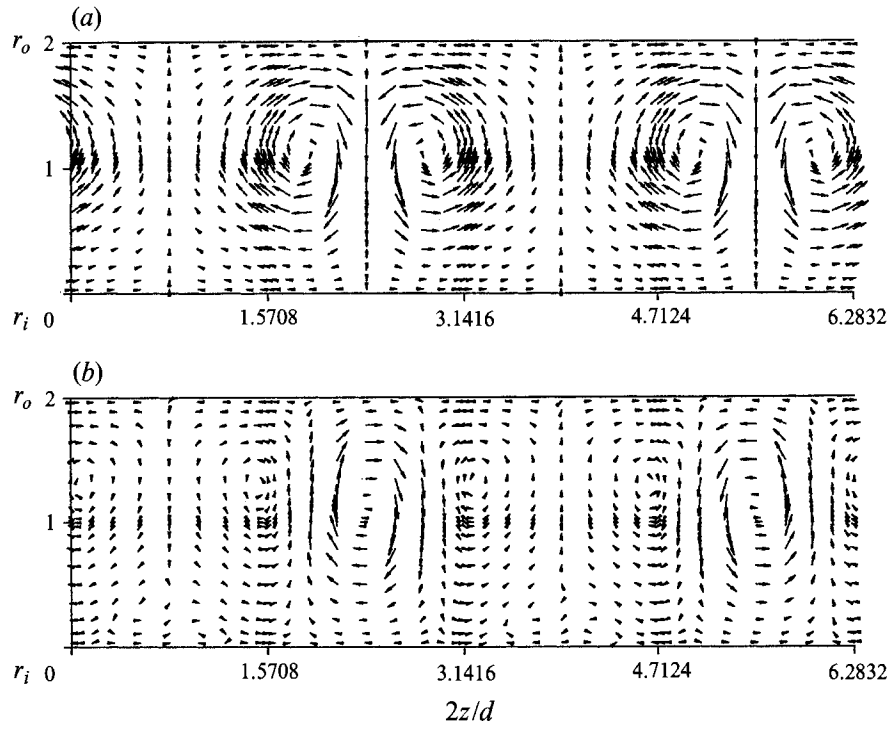

FIGURE 11. (*a*) Base Dean vortices ($\alpha = 2.0$) and (*b*) the related perturbation ($\beta = 1.0$) are projected onto the (r, z) plane at $\theta = 3.26$.

show that when the cosine function in (4.1) is replaced by a sine function, a perturbation pattern similar to that of the Dean case in figure 8 is observed. There is only one pair of perturbation vortices in the space of two base pairs. In all cases, no significant spanwise shift of the perturbation pattern is observed. In the Dean problem, a significant spanwise adjustment of the perturbation pattern is observed when the base Dean vortices enter the nonlinear stage (figure 7*b*). As a result, the perturbation pattern there is not sensitive to the spanwise phase difference between the base vortices and perturbation during the primary growth.

4.3. *Dean vortices with small wavenumber*

For base Dean vortices with long wavelength, the streamwise development of the perturbation and its relation to the energy level of base vortices are similar to those with short wavelength presented in §4.1. But the perturbation patterns on the cross-stream plane are quite different. Figures 11(*a*) and 11(*b*) show the flow patterns of the base flow and the perturbation at the downstream location $\theta = 3.26$. The parameters used to start the analysis are similar to those in figure 6 but the base Dean vortices having $\alpha = 2.0$ and the perturbation having $\beta = 1.0$ ($b = 0.5$). After the appearance of the Eckhaus instability, the number of vortices in the perturbation increases from one pair to three pairs (figure 11*b*), while the number of base vortices remains at two pairs (figure 11*a*). This situation is almost identical to that discussed in Guo & Finlay (1991). The superimposition of the perturbation on the base flow shows that near $2z/d = 0.8$, a small vortex pair with an inflow region at its centre is generated near the concave wall while the two old pairs with inflow regions at their centres near $2z/d = 2.4$ and 5.5 in

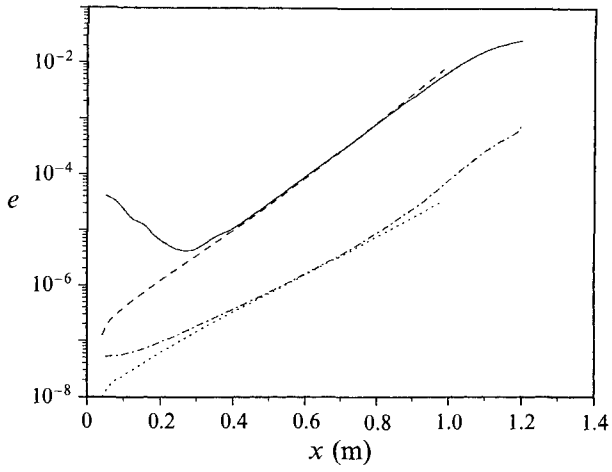

FIGURE 12. Energies of the base Görtler vortices $\lambda = 2.13$ cm ($A = 600$, ——) and the related perturbation $\lambda_1 = 4.26$ cm ($b = 0.5$) of spatial Eckhaus instability (—·—). The energies of linear Görtler vortices from primary instability with $\lambda = 2.13$ cm (– – –) and 4.26 cm (.....) are also given.

figure 11(*a*) are squeezed together towards $2z/d = 4.0$. In Guo & Finlay, the temporal simulations show that the nonlinear development of these perturbations results in the appearance of new vortex pair near $2z/d = 0.8$.

We find a similar result for base Dean vortices with other wavenumbers. If the fully developed Dean vortices are within the stability boundary of Eckhaus instability (i.e. they are stable and lie within the 'Eckhaus boundary' in Guo & Finlay 1991), we find that the growth of the perturbation is similar to that in figure 6 before the base Dean vortices reach the fully developed state. Once the base vortices become fully developed, the perturbation decays.

4.4. *Görtler vortices with long wavelength*

Figure 12 shows the energy of the Görtler vortices in the base flow with wavelength $\lambda = 2.13$ cm ($A = 600$) and the related perturbation of spatial Eckhaus instability with $\lambda_1 = 4.26$ cm ($b = 0.5$). Both the simulation code and the stability code are started at $x = 9.6$ cm with $\epsilon = 0.05$ in equation (4.1) but with the cosine function replaced by a sine function. For $0.4 < x < 0.7$ m, the base Görtler vortices are linear. When $x > 0.7$ m, the nonlinearity of the base Görtler vortices sets in, and the growth of the perturbation begins to differ from that of the primary instability, and the spatial Eckhaus instability begins to play an important role.

The evolution of the streamwise component u_θ^0 of the base Görtler vortices and the outflow component u_r' of the related perturbation is shown in figure 13. At $x = 0.52$ and 0.68 m, the patterns of the perturbation (figure 13*b*) are the same as the ones with $\lambda = 4.26$ cm from primary instability analysis. There is only one pair of vortices in the box. These perturbation patterns grow downstream until $x = 0.84$ m where the base Görtler vortices have reached a considerable nonlinear amplitude (figure 13*a*). At this location, two small additional single vortices begin to appear near the wall at the bottom of the two original vortices and continue to grow downstream. As in the case of short wavelength, the spanwise shift of the perturbation is very weak, and the downstream development of the perturbation depends sensitively on the phase difference between the base vortices and the perturbation before the onset of the Eckhaus instability. The effect of the perturbation on the base flow is similar to that

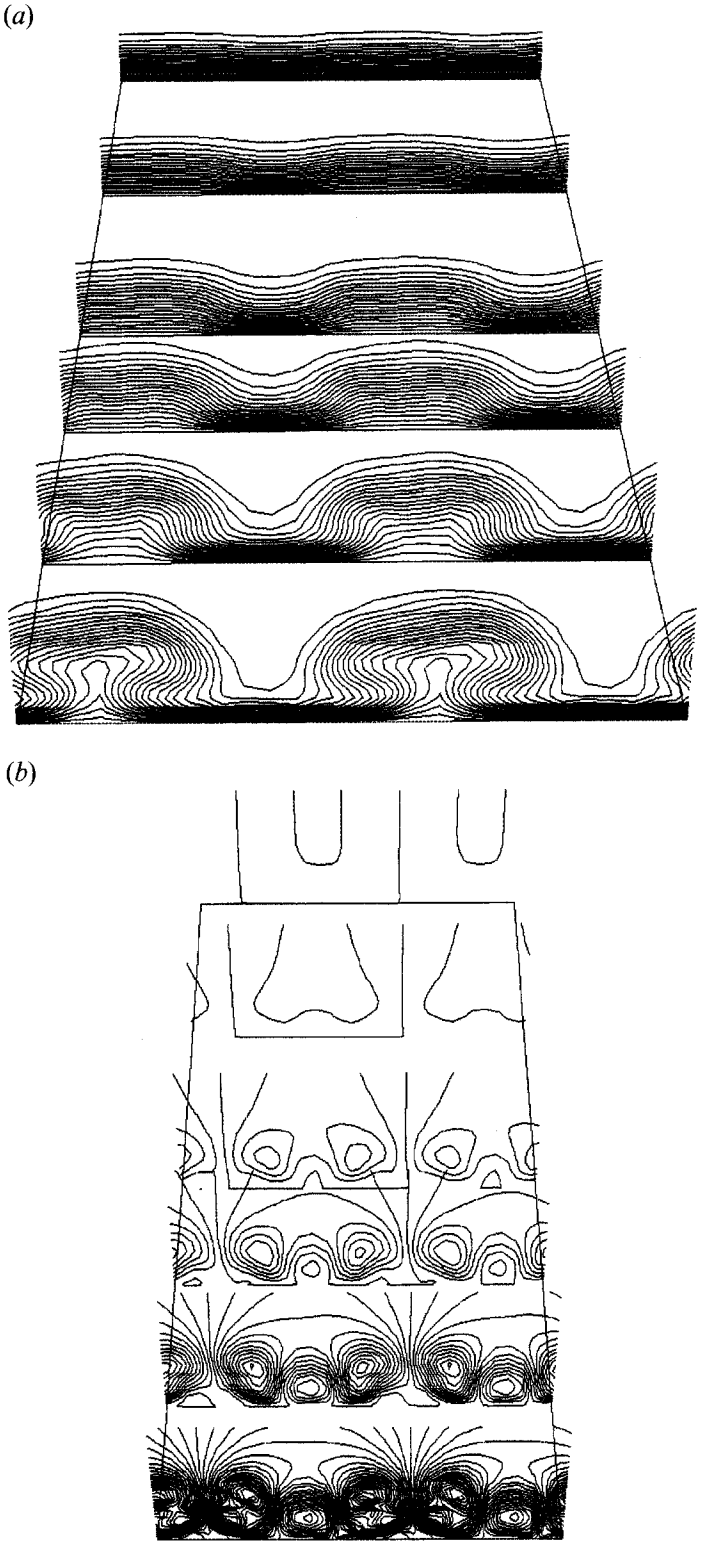

FIGURE 13. Contours of the velocity components (*a*) u_0^0 of the base Görtler vortices and (*b*) u_τ' of the perturbation in figure 12 are shown in cross-stream planes at $x = 0.52$, 0.68, 0.84, 0.93, 1.0 and

of Dean vortices with long wavelength: a new vortex pair will be created near the wall between the two existing vortex pairs which are squeezed together.

Figure 14 shows a similar case to that of figure 13 at $x = 0.984$ m but with the initial condition given by (4.1) and $\epsilon = 0.1$. Before the base vortices enter the nonlinear stage, the flow pattern of the perturbation is the same as the one in figure 13(*b*). When the base vortices become nonlinear at $x = 0.984$ m, the perturbation pattern shown in figure 14(*b*) is different from that in figure 13(*b*), although the total number of strong vortex pairs is still three. The superimposition of the perturbation on the base vortices shows that the effect of the perturbation on the base flow is similar to that in figure 13(*b*) except that the (small) new pair is closer to the vortex pair near $z/\lambda = 0.9$ than the other pair.

Similar results are found for all $\Lambda > 500$. The larger Λ is, the stronger the extra small vortice in the perturbation are, and the more likely it is that a new pair of vortices will appear in the flow. Like the Dean problem, it is difficult to define a lower bound on Λ at which the perturbation changes from having three pairs of vortices to one pair (and which thus distinguishes vortex splitting from merging).

4.5. *Some general features*

The perturbation flow patterns discussed in §§4.1–4.4 are typical patterns found in most cases. In all these cases, the perturbation wavenumber $b = 0.5$ is used. When other perturbation wavelengths ($b \neq 0.5$) are used, there are some differences between Dean and Görtler vortices. When Dean vortices reach a nonlinear stage and become fully developed, the growth rate σ and b exhibit a relation almost identical to that revealed by Guo & Finlay (1991) using a temporal theory, i.e. $b = 0.5$ gives the largest σ. This property has been discussed extensively in Guo & Finlay (1991) and we shall not repeat the discussion here. The nonlinear developing stage of the base Dean vortices serves as a transition zone for the energy of the primary instability to be transferred to the spatial Eckhaus instability. There also exists a wavenumber for a given *Re* which has the smallest growth rate of Eckhaus instability. This wavenumber is very close to that given by temporal theory (the 'Eckhaus valley' in Guo & Finlay 1991). In general, the growth rates of the spatial Eckhaus instability of fully developed Dean vortices are smaller than those of the primary instability. Table 1 lists typical values of these growth rates. It can be seen that they are almost eight times smaller than those of primary instability in most cases. Small growth rates suggest that in order to observe the splitting and merging of Dean vortices in a finite streamwise distance, relatively high energy levels of disturbances are needed. We will discuss this issue in §5.

In the case of Görtler vortices, the situation is a little different. Since the growth rate of spatial Eckhaus instability depends sensitively on the spanwise phase difference between the base vortices and the perturbation before the onset of the Eckhaus instability, and the growth of the nonlinear base Görtler vortices have different influences on Eckhaus instability with different b, it is difficult to compare the growth rates with different b and to determine the most unstable b. Only with the help of the simulations with a large spanwise computational box are we able to determine that $b = 0.5$ is the most unstable wavenumber in most cases. For example, when more than three pairs of Görtler vortices are included in a computational box, the splitting and merging of vortices mostly involves two pairs of Görtler vortices and the flow patterns are similar to those predicted by superimposing the perturbations with $b = 0.5$ on the

1.25 m. The concave wall is shown as a flat plate and the flow proceeds downstream from top to bottom. Contours: (*a*) 0:0.95 with contour increment 0.05. (*b*) $-0.000\,18$:0.000 18 with contour increment 0.9×10^{-5}.

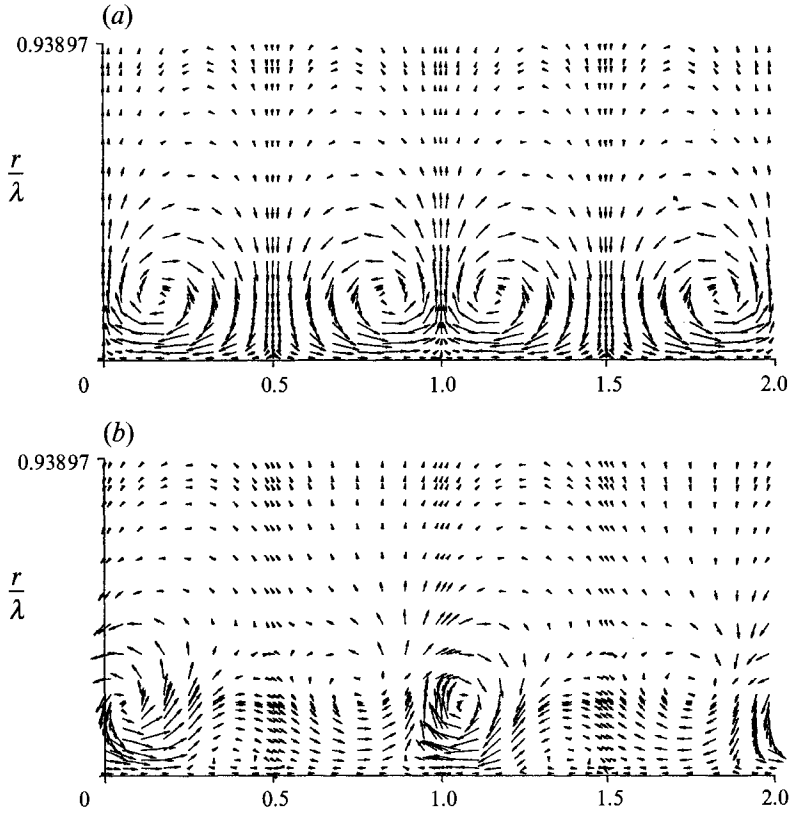

FIGURE 14. (*a*) Base Görtler vortices and (*b*) the perturbation with $\epsilon = 0.1$ in equation (4.1), are projected onto the (r, z)-plane at $x = 0.982$ m.

Re/Re_c	α	σ_{1D}	σ_{2D}
1.7	2.4	0.077	0.0124
1.9	2.4	0.091	0.0143
2.2	2.4	0.109	0.0156
2.5	2.4	0.122	0.0160
2.8	2.4	0.134	0.0180
3.0	2.4	0.140	0.0190
3.25	2.5	0.150	0.0200

TABLE 1. The growth rates of primary instability (σ_{1D}) and spatial Eckhaus instability (σ_{2D}) with $b = 0.5$ are listed as a function of Re/Re_c and wavenumber α

base Görtler vortices. Since the perturbation growth rate of spatial Eckhaus instability depends on the nonlinear development of the Görtler vortices in the base flow, it is difficult to define the growth rate of the spatial Eckhaus instability as a function of Görtler number G and wavelength parameter Λ. This is one of the problems facing the stability analysis of unsteady flow (Drazin & Reid 1981). Here, other than $b = 0.5$ being the most unstable, we give no specific growth rate pattern. Instead, we shall focus our attention on the physical consequences of this type of instability, for example vortex splitting and merging. This situation is different from the secondary instability of Tollmien–Schlichting waves reviewed by Herbert (1988), where the secondary

growth rate is much larger than that of the base Tollmien–Schlichting waves. The growth of the Tollmien–Schlichting waves has negligible effects on the secondary instability, and thus it is possible to present the growth rate of the secondary instability in the terms of the amplitude (percentage) of the base Tollmien–Schlichting waves.

To summarize the above discussions, our study in this section shows that when the energy level of the developing vortices in the base flow is low, the stability of each wavenumber is dictated independently by primary instability. Multiple wavenumbers can develop at the same time until a dominant wavenumber in the base flow reaches the nonlinear stage. As the dominant vortices develop nonlinearly, spatial Eckhaus instability sets in and the perturbations associated with the wavenumber $b = 0.5$ become the most unstable and continue to grow. The development of one wavenumber does not inhibit the development of other wavenumbers. Once the vortices are strongly nonlinear, the energy in wavenumbers other than the dominant one and its harmonics appears to be transferred from independently growing primary instability eigenfunctions into spatial Eckhaus instability eigenfunctions.

5. Simulation of vortex splitting and merging

To support the arguments and results from linear theory in §4, we study in this section the nonlinear aspects of spatial Eckhaus instability using the simulation code. For Dean vortices, the initial flow conditioins used to start the simulation code are

$$\boldsymbol{u} = (0, u_{1D}(1.0 + (\sin(4\pi\alpha z) + \epsilon \sin(4\pi\beta z)) \times 10^{-4}), 0), \tag{5.1}$$

where α is the wavenumber of the dominant Dean vortices and β is the perturbation wavenumber. Here, the dominant vortices α correspond to the base vortices in a linear theory and the perturbation β simulates the perturbation of Eckhaus instability. In the case of Görtler vortices, the initial conditions are

$$\boldsymbol{u} = (v_B, u_B + 0.03u_B(\sin(4\pi z/\lambda) + \epsilon \sin(4\pi z/\lambda_1)), 0), \tag{5.2}$$

where λ is the dominant wavelength, λ_1 is the perturbation wavelength. In (5.1) and (5.2), ϵ is used to adjust the energy level of the perturbation relative to the dominant vortices. Two pairs of dominant vortices are included in the computational box since, in all cases studied, the most unstable perturbation wavenumber b is 0.5 or 1.5. We also monitor the energy in spanwise Fourier mode k_z defined by (Finlay *et al.* 1988)

$$E(k_z) = c(k_z) \int_{r_i}^{r_0} \hat{\boldsymbol{u}}(r, k_z)^2 \, \mathrm{d}r,$$

where $c(k) = 0.5$ for $k = 0$ and $c(k) = 1$ for $k \neq 0$; $\hat{\boldsymbol{u}}(r, k_z)$ is the spanwise Fourier transform of $\boldsymbol{u}$. In the case of $b = 0.5$, before the spanwise perturbation becomes nonlinear the energy in the first mode comes mostly from the perturbation with $b = 0.5$ and the energy in the second mode comes mostly from the dominant vortices.

5.1. *Dean vortices with large wavenumber*

Figure 15 shows the flow pattern in cross-stream planes of a flow with the dominant wavenumber $\alpha = 4.0$ and the perturbation wavenumber $\beta = 2.0$ ($b = 0.5$). In this simulation, $\epsilon = 0.08$. Two pairs of the dominant Dean vortices becomes visible at $\theta = 2.75$. At $\theta = 3.0$, they are fully developed. A complete vortex merging event can be seen at $\theta = 4.25$ shortly after the dominant wavenumber reaches the fully developed

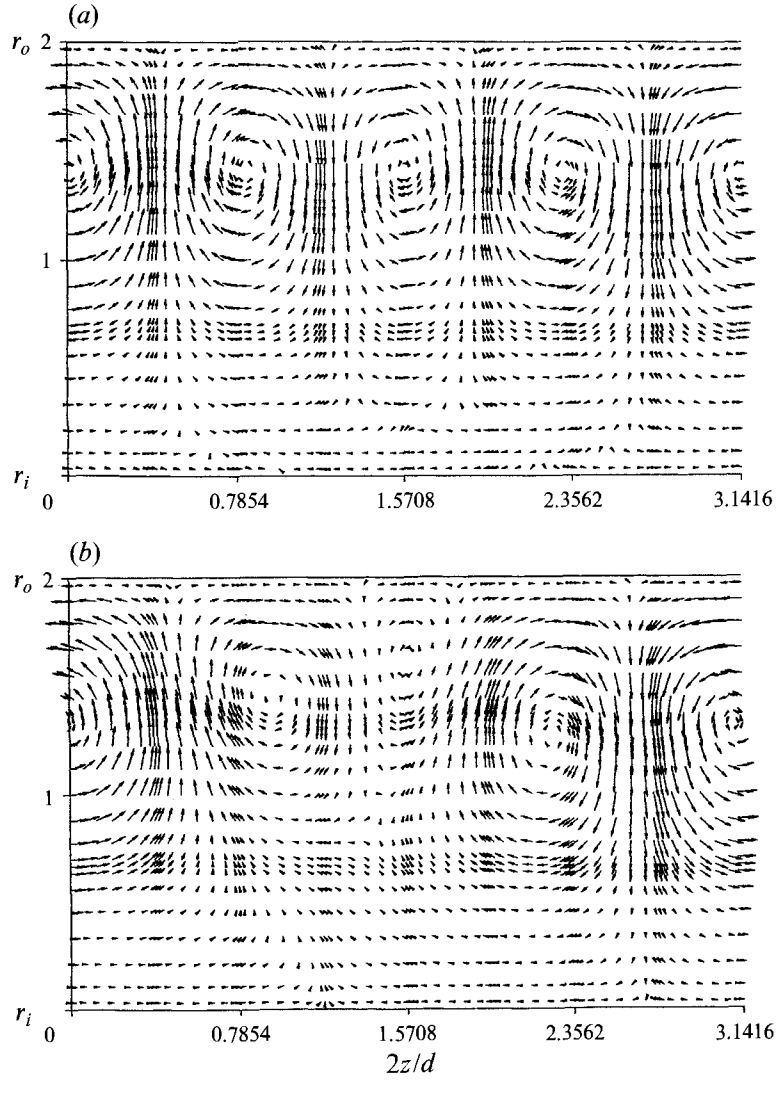

FIGURE 15(*a*,*b*). For caption see facing page.

state. At $\theta = 1.51$ in figure 15(*a*), there are two pairs of vortices with outflow regions at their centres near $2z/d = 1.2$ and 2.7. At this stage, the vortices are basically linear. Both pairs have almost the same strength. At $\theta = 3.01$ in figure 15(*b*), the dominant vortices are more or less fully developed. We can see that there are some distortions on the vortex pair near $2z/d = 1.2$. We believe these distortions are due to the growth of the energy associated with the perturbation $\beta = 2.0$. These distortions provide high perturbation levels for the nonlinear development of spatial Eckhaus instability that soon follows. At $\theta = 3.76$ in figure 15(*c*), the vortex pair between $2z/d = 1.6$ and 2.4 is squeezed towards $2z/d = 2.0$ and becomes smaller, while the other vortex pair grows bigger. This development continues downstream. At $\theta = 4.81$ in figure 15(*d*), the two small vortices near $2z/d = 2.0$ in figure 15(*c*) disappear completely and there is only one pair of vortices in the domain. The vortex merging event is completed.

The energy development of figure 15 is shown in figure 16. We can see that before

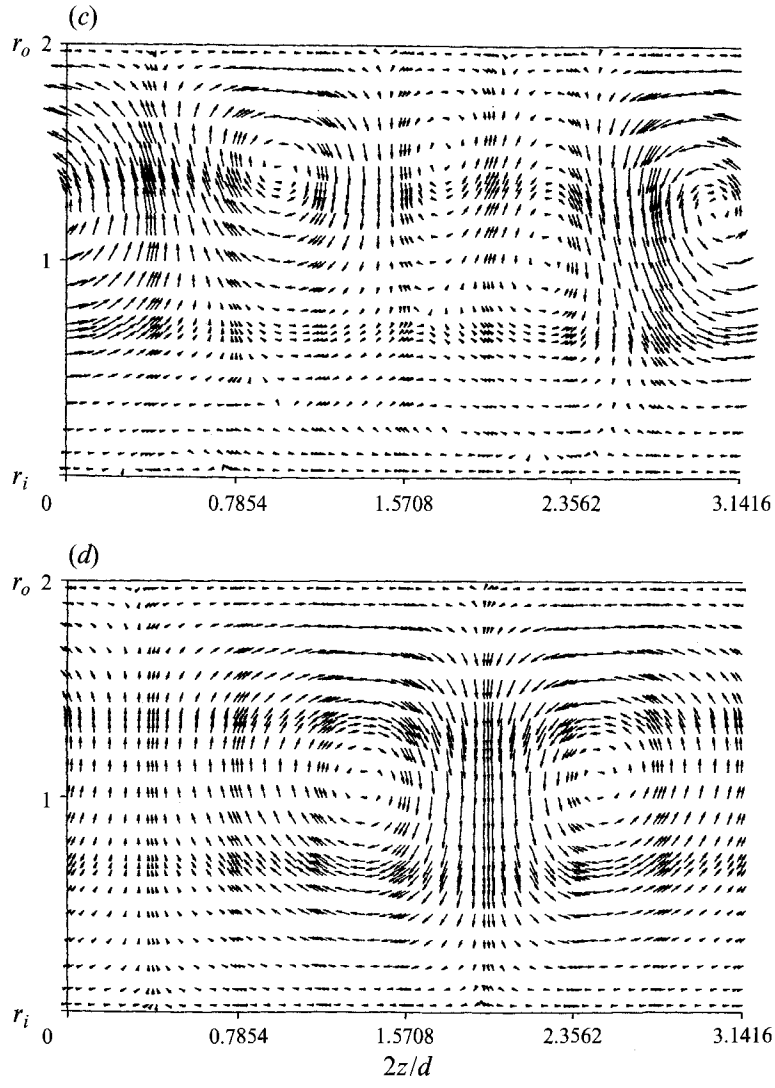

FIGURE 15. Dean vortices in a curved channel $\gamma = 0.975$ at $Re = 2.0Re_c$ are projected onto the (r, z)-plane at (*a*) $\theta = 1.51$; (*b*) $\theta = 3.01$; (*c*) $\theta = 3.76$ and (*d*) $\theta = 4.81$ rad. The simulation is started with $\alpha = 4.0$, $\beta = 2.0$ and $\epsilon = 0.08$ in equation (5.1).

the energy in the second Fourier mode reaches the nonlinear state at $\theta = 2.0$, the energy growth rates in the second and first modes are 0.07 and 0.09, which are equal to the growth rates of primary instability at $\alpha = 4.0$ and 2.0. Before the Dean vortices in the base flow reach a nonlinear level, the growth of each wavenumber is governed purely by primary instability. When the dominant Dean vortices enter the nonlinear stage at $\theta = 2.0$, the growth of the second and first modes begins to slow down. When the dominant wavenumber reaches the fully developed state at $\theta = 3.5$, the energy in the first mode continues to grow from $\theta = 3.5$ to 4.0 but at the new rate 0.02, which is close to the growth rate of spatial Eckhaus instability of fully developed Dean vortices $\alpha = 4.0$ (cf. figure 6). Further downstream, nonlinear interaction between the dominant wavenumber and the perturbation can be expected because the energy level

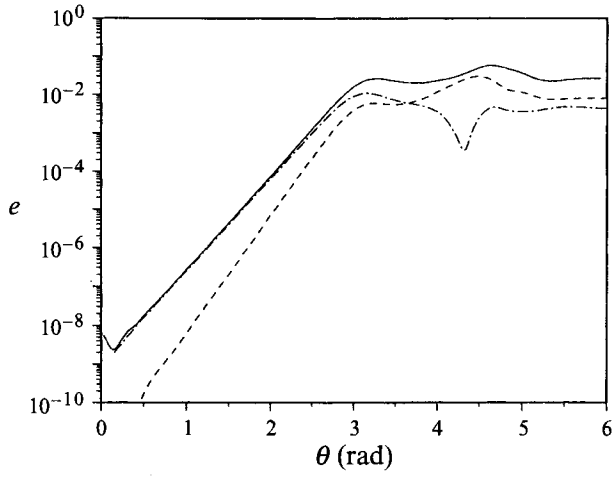

FIGURE 16. Spatial variation of the total energy (——) and the energies in the first (– – –) and the second (—·—) spanwise Fourier modes of the Dean vortices in figure 15.

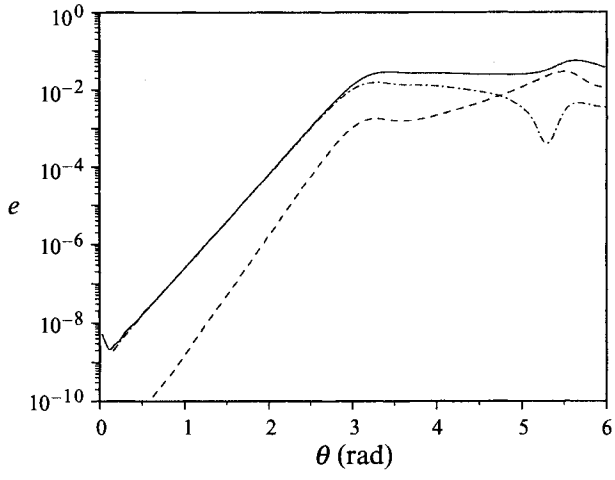

FIGURE 17. Energy of a flow similar to that in figure 16 but with $\epsilon = 0.05$ in equation (5.1).

in the first mode is comparable with that in the second mode. At $\theta = 4.25$, the sudden drop of energy in the second mode indicates the beginning of nonlinear vortex merging.

Comparing figure 15(*c*) to the linear stability analysis in §4.1, we can see that the merging event roughly follows what is predicted by the stability theory: one vortex pair separated by an outflow region is squeezed and weakened by Eckhaus instability, and eventually two pairs of vortices merge into one pair. From figures 15(*b*) and 15(*c*), we also see that the flow pattern switches from distorted Dean vortices to the vortex merging pattern predicted by the spatial Eckhaus theory.

During a vortex merging event, the vortex structures can become highly asymmetric and irregular due to the nonlinear development of spatial Eckhaus instability and the nonlinear interactions between different wavenumbers. But when the merging event is complete, the vortex structures become symmetric again. In experiments, time-dependence of the flow will probably occur due to time-varying inlet perturbation conditions. How this will affect vortex merging process needs further study.

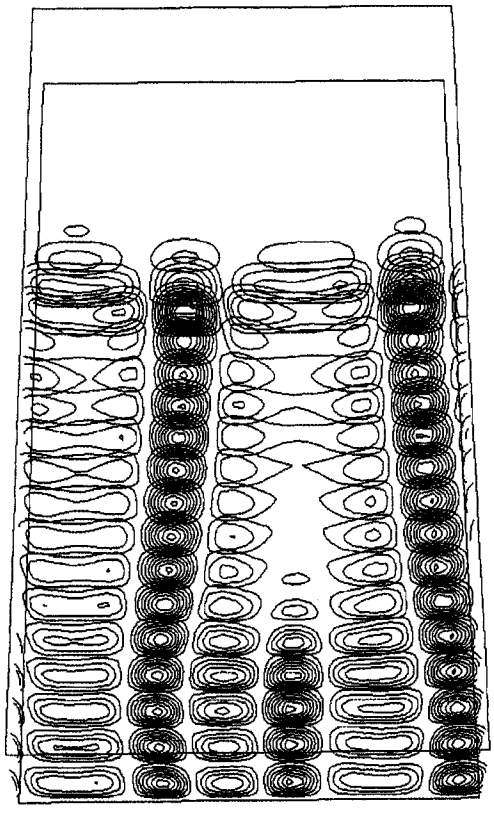

FIGURE 18. Contours of the velocity component u_r of developing Dean vortices is shown in cross-stream planes from the streamwise location $\theta = 0.255$ to 6 rad with $\Delta\theta = 0.25$ rad in a curved channel with $\gamma = 0.975$ at $Re = 2.186Re_c$. The simulation is started with $\alpha = 2.0$, $\beta = 3.0$ and $\epsilon = 0.25$ in equation (5.1). The inner wall is above the outer wall and the flow proceeds downstream from top to bottom. Contours: $-0.1 : -0.01$, $0.01 : 0.1$ with contour increment 0.01.

We can control the streamwise location of a vortex merging event by adjusting ϵ in equation (5.1). Figure 17 shows the development of the energy for a flow similar to that in figure 16, but now with $\epsilon = 0.05$. It can be seen more clearly that the energy growth rate of the first Fourier mode switches from the primary growth rate $\sigma = 0.09$ when $\theta < 2.0$ to the growth rate $\sigma = 0.02$ of spatial Eckhaus instability when $\theta > 3.5$. The merging event is completed by $\theta = 5.5$. Our simulations show that when small ϵ is used, the dominant Dean vortices are less distorted when their amplitude saturates and the structures of the vortices are more symmetric, like those in Guo & Finlay (1991, figure 19). In addition, the merging event takes a longer streamwise distance to complete when a smaller ϵ is used.

5.2. *Dean vortices with small wavenumber*

Figure 18 shows the evolution of the velocity component u_r of a flow where the dominant wavenumber is $\alpha = 2.0$ and the perturbation wavenumber is $\beta = 3.0$ ($b = 1.5$) and $Re = 2.186Re_c$. In this simulation, $\epsilon = 0.25$. We choose $b = 1.5$ here instead of $b = 0.5$ because the growth rate of the primary instability at $\beta = 3.0$ is larger than that at $\beta = 1.0$ ($b = 0.5$). When the dominant wavenumber enters the nonlinear stage, the growth rate of the spatial Eckhaus instability is the same for both $b = 1.5$ and 0.5 (cf. (3.1)). Thus, $b = 1.5$ will generate more disturbance energy than $b = 0.5$ will

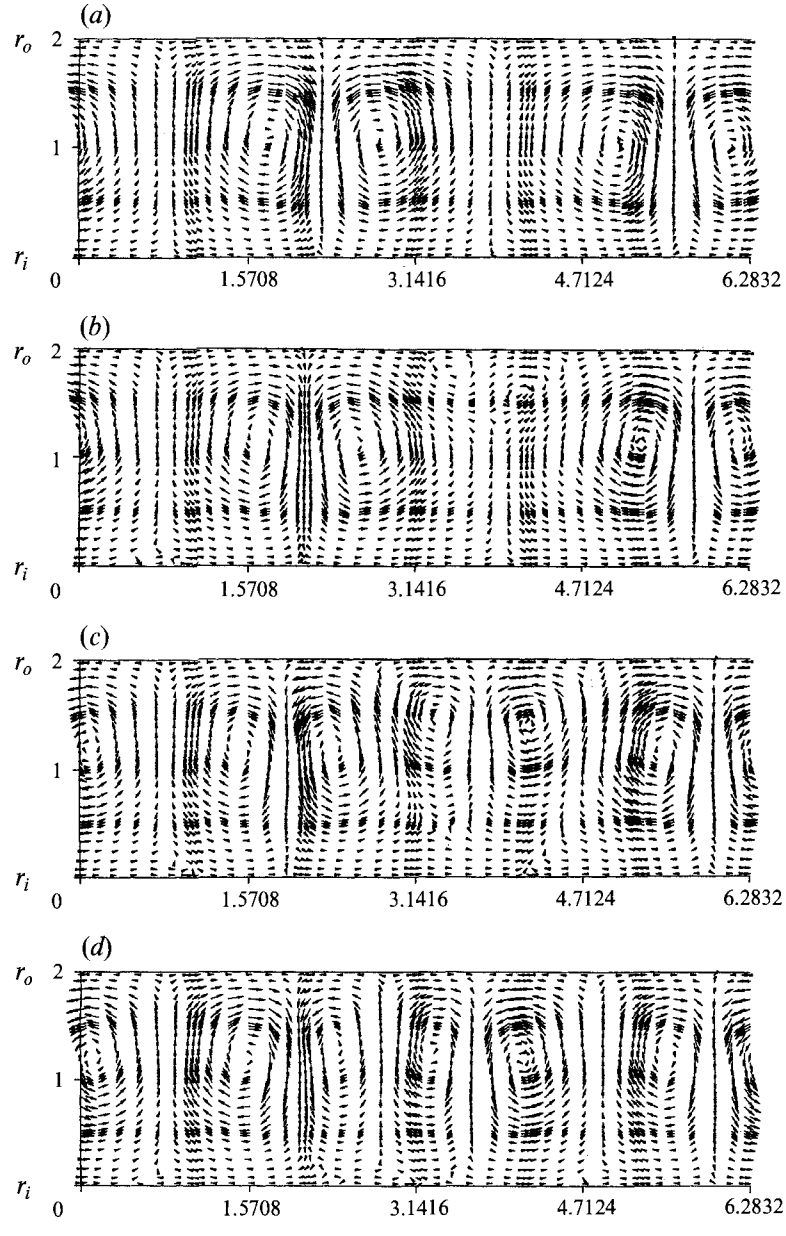

FIGURE 19. Dean vortices of figure 18 are projected onto the (r, z)-plane at (*a*) $\theta = 2.5$; (*b*) $\theta = 4.0$; (*c*) $\theta = 5.0$ and (*d*) $\theta = 6.0$ rad.

when entering the Eckhaus instability stage (a simulation with $b = 0.5$ confirms this). In figure 18, it can be seen that the two dominant vortex pairs reach a fully developed stage at $\theta = 2.25$. Shortly afterwards at $\theta = 4.0$, a new vortex pair appears between the two dominant vortex pairs and the dominant pairs are pushed apart a little. For $\theta > 4.5$, the domain is filled by three pairs of vortices. This is a vortex splitting event.

The flow pattern of figure 18 is shown in cross-stream planes in figure 19. At $\theta = 2.5$ in figure 19(*a*), there are two equal-strength pairs of vortices with inflow regions near $2z/d = 1.8$ and 5.8. Downstream at $\theta = 4.0$ in figure 19(*b*), the two dominant pairs are pushed apart and a small vortex pair can be seen at $2z/d = 3.9$ near the

concave wall. This new vortex pair has an inflow region at its centre. As this new vortex pair grows downstream, it pushes the two dominant pairs further apart in figure 19(*c*). By $\theta = 6.0$ in figure 19(*d*), the vortex splitting event is complete and three pairs of vortices occupy the whole domain. We can see that the vortex splitting pattern is well predicted by linear stability theory in §4.3. A small new vortex pair is generated first near the concave wall in between two dominant vortex pairs. It has an inflow region at its centre. Two dominant vortex pairs are pushed apart by the new pair.

The development of the energy in spanwise Fourier modes shows a similar situation to those in figures 15 and 17, except that here the energy in the third Fourier mode is used to monitor the growth of the perturbation with $b = 1.5$. As in the case of vortex merging, the streamwise location of a vortex splitting event can be controlled by adjusting ϵ in (5.1). An increase in ϵ causes a splitting event to become visible earlier upstream.

5.3. *Görtler vortices with short wavelength*

Figure 20 shows the flow patterns in the cross-stream plane of a simulation with the dominant wavelength $\lambda = 0.749$ cm ($\Lambda = 125$) and the perturbation wavelength $\lambda_1 = 2\lambda$ ($b = 0.5$). The simulation is started at the streamwise location $x = 0.032$ m. A relatively large ϵ ($\epsilon = 0.2$) is used in (5.2). Figure 20(*a*) shows the flow pattern at $x = 0.556$ m. There are two pairs of relatively weak vortices in the domain. Further downstream at $x = 0.71$ m, the vortex pair with an outflow region near $z/\lambda = 1.75$ grows bigger in the r-direction compared with the other pair centred near $z/\lambda = 0.8$. These changes are seen more clearly at $x = 0.864$ m in figure 20(*c*). The flow patterns in figure 20(*c*) and figure 10(*c*) are quite similar. The lower half of the vortex pair near $z/\lambda = 1.75$ in figure 20(*c*) is squeezed together while the upper half is elongated in the r-direction and grows bigger. The vortex pair near $z/\lambda = 0.8$ is pressed towards the wall (relative to the growing boundary-layer thickness) and becomes shorter in the r-direction but wider in the spanwise direction. This vortex merging pattern continues to develop nonlinearly downstream. At $x = 1.018$ m (figure 20*d*), the vortex pair near $z/\lambda = 1.75$ is much stronger and elongated in the r-direction, while the other pair near $z/\lambda = 0.8$ grows only a little in the r-direction. Further downstream at $x = 1.171$ m in figure 20(*e*), as the vortex pair near $z/\lambda = 1.75$ moves away from the wall, its strength reduces. The vortex pair near $z/\lambda = 0.8$ becomes stronger again. Our simulation shows that further downstream, this vortex pair eventually occupies the whole domain and the vortex pair near $z/\lambda = 1.75$ disappears totally as it moves away from the wall.

The energies in the first and second Fourier modes of the Görtler vortices in figure 20 are shown in figure 21, together with the perturbation energy of the spatial Eckhaus instability. The perturbation energy level is scaled to match the energy in the first Fourier mode. It can be seen that for $x < 0.6$ m, the energy in the second Fourier mode (which corresponds to the dominant wavelength) is close to the total energy. This indicates that the dominant Görtler vortices are in the linear stage and the energy in the harmonics of the dominant wavelength is negligible. When $x > 0.6$ m, the energy in the second mode begins to drop (compared to the total energy) and the nonlinearity of this dominant wavelength begins to set in. For $0.45 < x < 0.6$ m, the growth of the first mode is roughly predicted by spatial Eckhaus instability. When $x > 0.6$ m, the growth of the first mode begins to slow down. By $x > 0.9$ m, the energy level in the first mode is quite comparable with that in the second mode. From figure 20(*c*), we know that the nonlinear development of the spatial Eckhaus instability begins to dominate the flow at this point, and the interactions among different wavelengths become visible.

Generally, the smaller ϵ is, the greater streamwise distance over which the prediction given by spatial Eckhaus instability for the energy growth in the first mode is valid.

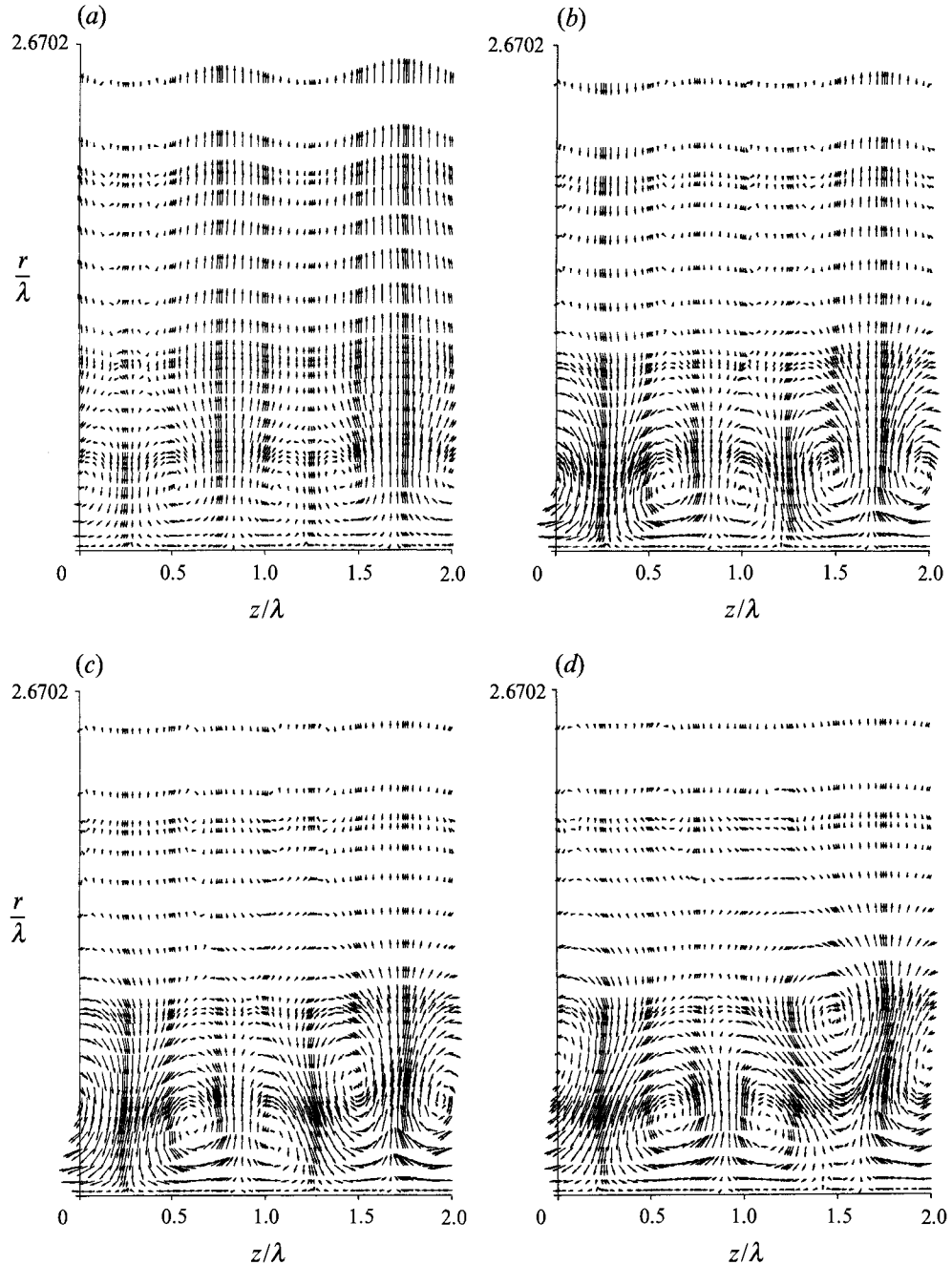

FIGURE 20(*a–d*). For caption see facing page.

This situation is similar to that for Dean vortices. It is not surprising that the linear prediction fails once nonlinearity sets in. When ϵ is large, nonlinearity occurs early and there are three types of nonlinearities involved: the nonlinearity of the dominant vortices, the nonlinearity of perturbations and the nonlinear interaction between the dominant vortices and perturbations. It is difficult to determine these nonlinear effects even with numerical simulations.

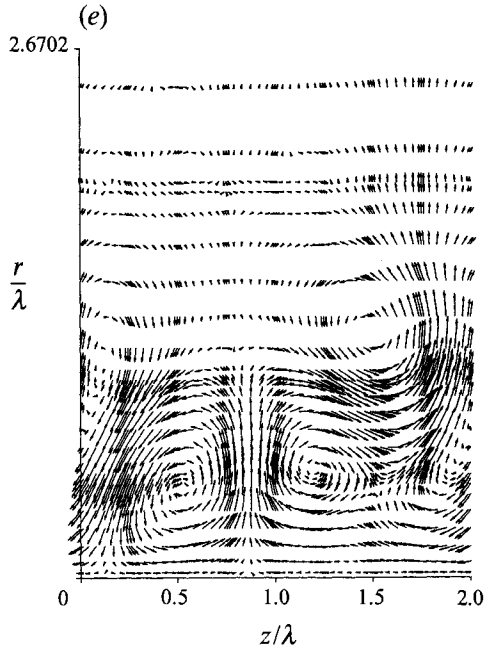

FIGURE 20. Görtler vortices with dominant wavelength $\lambda = 0.749$ cm ($\Lambda = 125$) are projected onto the (r, z)-plane at (*a*) $x = 0.556$ m; (*b*) $x = 0.71$ m; (*c*) $x = 0.864$ m; (*d*) $x = 1.018$ m and (*e*) $x = 1.171$ m. Here, $U_\infty = 5\ \mathrm{m\ s^{-1}}$. $\nu = 14.5 \times 10^{-6}\ \mathrm{m\ s^{-2}}$ and $R = 3.2$ m. The simulation is started with $\lambda = 0.749$ cm, $b = 0.5$ and $\epsilon = 0.2$ in equation (5.2).

Compared to Dean vortices, the vortex merging process of Görtler vortices is a little different. In the case of Dean vortices, once a vortex pair separated by the fluid flowing towards the concave wall is squeezed together and becomes smaller, this flow pattern continues to develop until the squeezed pair totally disappears. In the case of Görtler vortices, one vortex pair is pressed towards the wall and becomes shorter in the r-direction (relative to the undistorted case), while its neighbouring pair is elongated in the r-direction and grows bigger. Further downstream as this neighbouring vortex pair moves away from the wall and becomes weaker (probably due to a reduction of the centrifugal force which drives the centrifugal instability), the remaining vortex pair begins to dominate the domain. This phenomenon is not found in Dean vortices where the vortices occupy the whole breadth of the channel and the convex wall prevents any escape. But in both Dean and Görtler vortices, the nonlinear vortex merging patterns are quite similar to those predicted by spatial Eckhaus instability theory.

5.4. *Görtler vortices with long wavelength*

Figure 22 shows the spatial development of the velocity component u_θ of a simulation with the dominant Görtler vortices with $\lambda = 2.13$ cm ($\Lambda = 600$), the perturbation $\lambda_1 = \frac{2}{3}\lambda$ ($b = 1.5$), and the perturbation level $\epsilon = 0.8$. The two dominant mushrooms can first be seen at $x = 0.474$ m. They grow rapidly downstream. At $x = 0.627$ m, a small mushroom can be detected in between the two dominant mushrooms. By $x = 0.781$ m, the small mushroom is clear. It is closer to the right dominant mushroom than to the left one. Adjusting ϵ, we can control the streamwise location of the appearance of the new pair of vortices. In figure 22, a very large $\epsilon = 0.8$ is used. If we increase the wavelength of the dominant Görtler vortices to $\lambda = 2.5$ m, a smaller

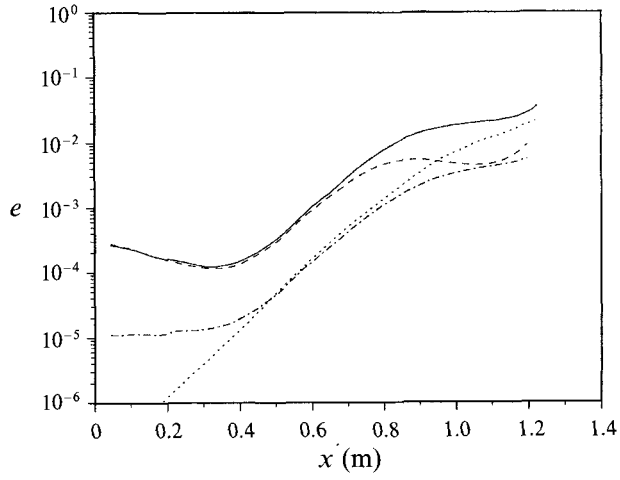

FIGURE 21. The total energy (——) and the energies in the first (— · —) and second (– – –) Fourier mode of the Görtler vortices in figure 20 are shown *vs.* streamwise distance. Also given is the energy of the perturbation from spatial Eckhaus instability (.....).

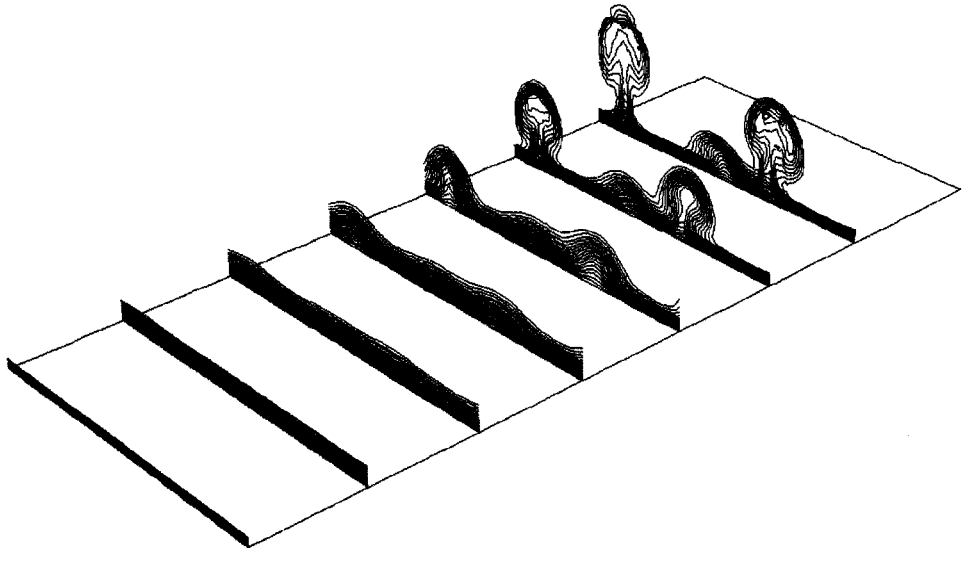

FIGURE 22. Contours of the streamwise velocity u_θ of the Görtler vortices with dominant wavelength $\lambda = 2.13$ cm ($\Lambda = 600$) are shown in cross-stream planes from $x = 0.0384$ to 0.96 m with $\Delta x = 0.1536$ m. Here, $U_\infty = 5$ m s^{-1}, $\nu = 14.5 \times 10^{-6}$ m s^{-2} and $R = 3.2$ m. The simulation is started with $\lambda = 2.13$ cm, $b = 1.5$ and $\epsilon = 0.8$ in equation (5.2). The concave wall is shown as a flat plate and the flow proceeds downstream from left to right. Contours: 0:0.9 with contour increment 0.05.

$\epsilon = 0.2$ is enough to make the vortex splitting quite visible in the same streamwise distance.

The flow pattern at $x = 0.93$ m of figure 22 is shown in figure 23. In addition to two dominant Görtler vortices with outflow regions near $z/\lambda = 0.6$ and 1.8, there is also a small vortex pair near $z/\lambda = 1.25$. In the spanwise direction, there are three vortex pairs in the domain. The flow pattern in figure 23 is roughly predicted by the linear stability theory in §4.4 (in the case of figure 14). The new vortex pair is generated near

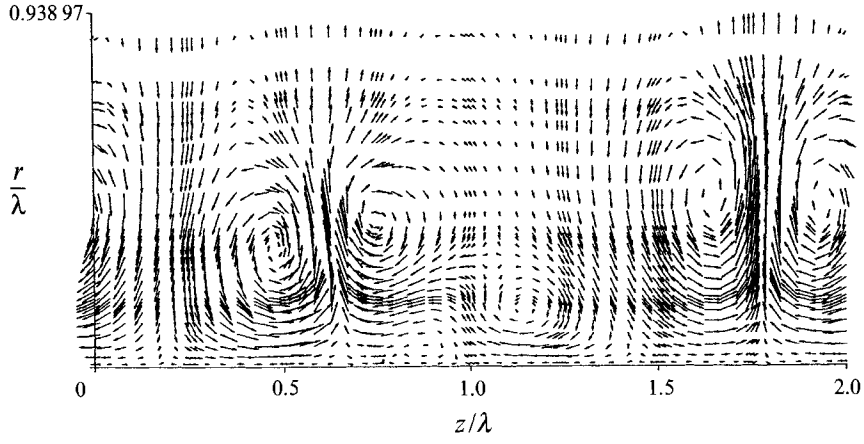

FIGURE 23. Görtler vortices of figure 22 are projected onto the (r, z)-plane at $x = 0.934$ m.

the wall in between the two dominant vortex pairs in a region where the fluid flows towards the wall, and is closer to one dominant pair than the other.

5.5. *General discussion*

Similar results are also found at other parameter values. In the case of Dean vortices, the instability of developing Dean vortices to spanwise perturbations is essential for vortex splitting or merging to be observed at a finite downsteam distance. Initial perturbations at the channel entrance, as well as the growth rates of the primary instability and the spatial Eckhaus instability all play important roles in the first appearance of vortex splitting or merging.

In the case of Görtler vortices, both splitting and merging types of nonlinear development of spatial Eckhaus instability significantly modify the mushroom shapes of the streamwise velocity and cause asymmetric vortex structures and irregularity. Since most Görtler vortices break down for $x > 1.2$ m for the flow parameters we have used (cf. Swearingen & Blackwelder 1987), the nonlinear development of splitting and merging of vortices may not have sufficient streamwise distance to develop fully. For example, in the case of vortex merging, the Görtler vortices will probably break down before two vortex pairs develop completely into one pair. Thus, in experiments only the beginning of the merging process is likely to be observed. Because Görtler vortices are under constant spatial evolution, vortex splitting may manifest itself through the later formations of some vortex pairs in between other vortices. If we consider an observation of one vortex pair becoming smaller while its neighbour grows bigger as the signature of vortex merging, and the later appearance of some vortices in between existing vortices as the signature of vortex splitting, then experimental evidence is plentiful (cf. Bippes 1972; Aihara & Koyama 1980; Aihara *et al.* 1984; recently Swearingen & Blackwelder 1987). Our recent conversation with H. Bippes further confirms this. Since there are severe irregularities in most experimentally observed Görtler vortices and no special attention has been given to the spatial Eckhaus instability of Görtler vortices, we will not elaborate on experimental evidence any further. We believe that the vortex splitting and merging or spatial Eckhaus instability can also be effectively studied experimentally by introducing two sets of disturbances near the leading edge: the first set has a larger amplitude and corresponds to the dominant wavelength λ in (5.2) and the second set corresponds to λ_1 in (5.2).

When perturbations with $b \neq 0.5$ (or 1.5) are used, results similar to those discussed in §§5.1–5.4 are obtained if the perturbation energy level is much lower than that of the dominant vortices and there is no nonlinear interaction between the perturbation and the dominant vortices. In other words, before the dominant vortices become fully developed, the growth of the perturbation with low energy level is governed by primary instability. When the dominant vortices are fully developed, the growth rate of this perturbation is given by spatial Eckhaus instability. If the perturbation level is high and comparable with that of the dominant vortices, some energy of the perturbation with $b \neq 0.5$ is converted into perturbations with b near 0.5 due to nonlinear interactions between the dominant vortices and the perturbations with $b \neq 0.5$. As a result, the growth of the perturbation with $b = 0.5$ dominates the flow in some cases and the nonlinear vortex splitting and merging discussed early in this section occur. If the growth of the perturbation with $b = 0.5$ does not dominate the flow, vortex splitting and merging still occur but in a different (irregular) way. In the case of Dean vortices, spatial Eckhaus instability is still characterized by vortex splitting and merging. And in the case of Görtler vortices, it is characterized by irregularities of the dominant Görtler vortices.

Compared to Dean vortices, Görtler vortices have a smaller growth rate of spatial Eckhaus instability. In order to observe vortex splitting and merging (in figures 20 and 22), a large ϵ is required. This indicates that the interactions between Görtler vortex pairs are not as strong as those between Dean vortices.

6. Wavenumber selection and irregularity

6.1. *Dean vortices*

From spatial primary stability theory (cf. Matsson & Alfredsson 1990), we know the growth rates of primary instability do not vary significantly with α for a band of wavenumbers near the one with the maximum growth rate. The wavenumber selection mechanism of primary instability is not strong for this band of wavenumbers. Since the nonlinear growth of Dean vortices depends on both the growth rate of primary instability and the perturbations at the entrance of a channel, the wavenumber with the maximum growth rate is not necessarily the one that will be observed in experiments. The observed wavenumbers could be in a band near the most unstable wavenumbers, especially for high Re where the differences between the primary growth rates for different wavenumbers are small. If the perturbations have equal energy for all wavenumbers (e.g. low-level broadband turbulence), then upstream of any vortex splitting or merging event, the observed wavenumber should be close to the one with the maximum growth rate. At high Re ($> 2.0Re_c$), the spatial development of Dean vortices is very sensitive to small disturbances due to a large primary growth rate. For example at $Re = 2.186Re_c$, our simulation shows that a perturbation level less than $10^{-5}\bar{U}$ is enough to make Dean vortices visible at a streamwise distance of $\theta < 5.0$ rad. Thus we believe that the preference of Dean vortices for certain spanwise locations observed by Matsson & Alfredsson (1992) may be due to disturbances caused by the channel geometry.

In §§4 and 5, we have shown that the developing Dean vortices are unstable to spanwise perturbations. The nonlinear growth of these spanwise perturbations causes vortex merging and splitting. As a result, the wavenumbers of Dean vortices are changed. Since the first round of vortex splitting and merging events depends on the initial perturbations at the channel entrance and the growth rates of primary instability and spatial Eckhaus instability, it is difficult to predict the favoured wavenumbers that

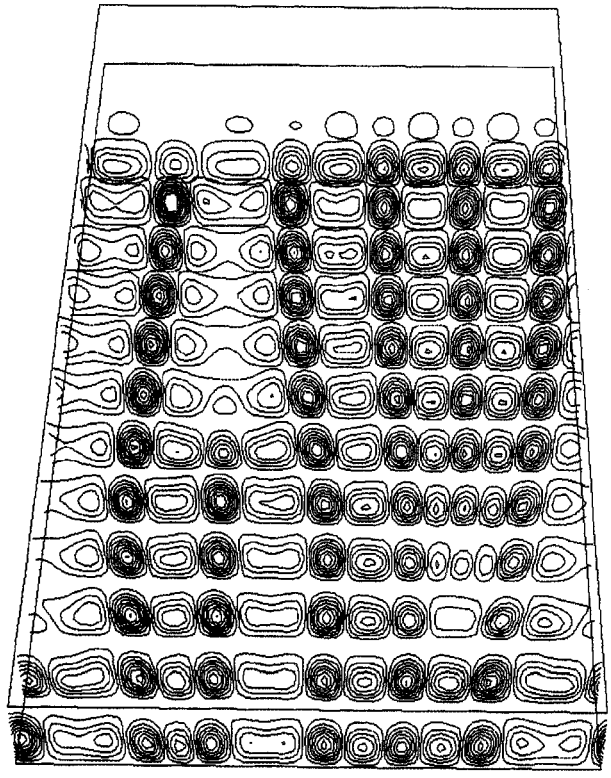

FIGURE 24. Contours of the velocity component u_r of developing Dean vortices is shown in cross-stream planes from the streamwise location $\theta = 0.5$ to 7.5 rad with $\Delta\theta = 0.5$ rad in a curved channel $\gamma = 0.975$ at $Re = 2.186Re_c$. The simulation is started with $\alpha = 3.0$ for the right three vortex pairs and $\alpha = 2.5$ for the left two vortex pairs. The inner wall is above the outer wall and the flow proceeds downstream from top to bottom. Contours: $-0.08 : 0.08$ with contour increment 0.0105.

survive the first round of vortex splitting and merging. Further downstream as the splitting and merging of vortices continues to occur due to the instability of nonlinear Dean vortices with respect to spanwise perturbations, the wavenumbers that have the minimum growth rate of spatial Eckhaus instability are more likely to be observed. More discussion on this wavenumber selection mechanism can be found in Guo & Finlay (1991).

The perturbations needed for splitting and merging of vortices to occur can also come from the interactions between vortices with different wavenumbers. Figure 24 shows such a case at $\gamma = 0.975$ and $Re = 2.186Re_c$. The initial perturbations used to start the simulation have a wavenumber of 2.5 for the left two vortex pairs and 3.0 for the remaining three vortex pairs. The maximum amplitudes of the initial perturbations are 0.01 % $\bar{U}$. In figure 24, the Dean vortices of $\alpha = 3.0$ and 2.5 reach a fully developed state at $\theta = 2.5$. Then, near the two interfaces between vortices with different wavenumbers, a merging event among the vortices with $\alpha = 3.0$ and a splitting event among the vortices with $\alpha = 2.5$ begin to develop one after another. When the same parameters are used but with only one wavenumber initially in the flow, splitting or merging events are not visible in the same length of the channel.

Since Dean vortices are unstable all the time to spanwise perturbations for $Re > 1.5Re_c$ (outside the stability boundary of Eckhaus instability), they are constantly distorted by all other disturbances, e.g. the development of multiple wavenumbers

during their linear development and vortex splitting or merging during their nonlinear development. Observation of irregular Dean vortices should be rather common.

6.2. *Görtler vortices*

It has been shown by many researchers (cf. Floryan & Saric 1984; Hall 1983) that wavelengths near $\Lambda = 210$ generally have the largest primary growth rates. In Bippes' (1972) experiments when screens (disturbance generators) are used to generate isotropic random disturbances, the wavelength parameters Λ of the observed Görtler vortices are near 210. But in the observations of Tani (1962), Winoto & Crane (1980) and Swearingen & Blackwelder (1987), much longer wavelengths of naturally occurring Görtler vortices are observed ($\Lambda \geqslant 650$).

In Guo (1992), it has been shown that the growth rate of primary instability does not vary significantly from $\Lambda = 175$ to 400. For this wavelength range, the wavelength selection mechanism of primary instability is weak. It has also been shown by Hall (1983, 1988) that over a short distance downstream from the leading edge, the primary growth rate varies considerably for different forms of initial perturbations. This further widens the wavelength range favoured by primary instability, and thus weakens (and complicates) the wavelength selection mechanism of primary instability. If the perturbations near the leading edge are dominated by a wavelength within this widened wavelength range, this wavelength will have a better chance to develop into dominant vortices due to its higher initial energy level. If all wavelengths in the perturbations have equal energy, wavelengths near $\Lambda = 210$ are more likely to be observed due to their slightly higher primary growth rate in most cases.

Our simulations of nonlinear Görtler vortices in §5 show that the growth rates of primary instability are small compared to the streamwise length allowable for Görtler vortices to develop. Relatively high energy levels for initial perturbations (1% of U_∞) are required in our simulations in order to obtain Görtler vortices with a strength comparable with those observed by Swearingen & Blackwelder (1987). (In the case of Dean vortices, the initial perturbations are less than 0.001% of $\bar{U}$.) This suggests that in the experiments of Swearingen & Blackwelder, there exists a relatively high level of perturbations. According to the experimental specifications given by Swearingen & Blackwelder, these large perturbations are not in the free stream. At $x = 10$ cm from the leading edge, the disturbances they measured have amplitude 1% of U_∞. This indicates that somewhere in between the leading edge and $x = 10$ cm, large perturbations have been generated. These perturbations cannot be produced by a Görtler instability because of its small growth rate and the short streamwise distance to this location.

Since Bippes (1972) and Swearingen & Blackwelder (1987) observed different wavelengths for naturally occurring Görtler vortices, it is useful to compare the experimental devices of these two groups. In the experiments conducted by Swearingen & Blackwelder (1987), the test section is essentially a variable-width curved channel. The perpendicular distance between the testing (concave) plate and the convex plate is small. This design imposes restrictions on the vertical velocity u_r near the leading edge (where u_r is of order 1% of U_∞), and will generate perturbations that reduce the value of u_r compared with a free concave wall, i.e. perturbations with $u_r' = -\epsilon u_r$ (where u_r is the vertical velocity for a single free concave wall) will be generated. In Bippes' experiments, concave plates with constant curvature are towed in a water tank. We believe that this set-up imposes less restriction on the vertical velocity u_r near the leading edge. This is also manifested by the fact that when disturbance generators (screens) are not used in Bippes' experiments, the naturally occurring Görtler vortices

are very small and not well defined (Bippes, 1992, personal communication). Another likely source of large disturbances is the misalignment of the leading edge to the direction of the free-stream U_∞. Using the configurations of Swearingen & Blackwelder (1987), our simulations show that a misalignment of half a degree in the r- or z-direction will generate enough disturbances for the Görtler vortices of the observed strength to develop. The common feature of the large perturbations generated by either the restriction on u_r or misalignment of the leading edge to the free stream is that these large perturbations do not vary rapidly in the spanwise direction, and they depend strongly on the experimental apparatus. When random initial perturbations or perturbations with rapid spanwise variation are used in the simulations, we find the average wavelength of the dominant Görtler vortices is very close to $\Lambda = 210$, the one with the largest primary growth rate. In Bippes' experiments, the perturbations generated by screens are of rapid variation, so the observed wavelengths of Görtler vortices are close to $\Lambda = 210$.

From the above discussions we conclude that when the perturbations near the leading edge have both rapid and slow spanwise variations, there is energy in all wavelengths and thus the wavelength selection mechanism of primary instability plays a more important role. The wavelengths of the dominant Görtler vortices are expected to be close to $\Lambda = 210$. When the perturbations near the leading edge have only slow spanwise variation, longer wavelengths will be favoured and the dominant Görtler vorties will have wavelengths longer than $\Lambda = 210$.

Another important source of large perturbations is the leading edge itself. When the free stream hits the leading edge, acoustic waves will be generated and the flow near the leading edge is elliptic in nature. To determine the form and strength of disturbances generated by the leading edge, it is probably necessary to resort to a time-dependent, three-dimensional elliptical analysis. Very recently, attention has been given to the leading-edge receptivity of the Görtler problem (Hall 1990). Readers are referred to Hall (1990) for more details.

The studies in §§4 and 5 show that developing Görtler vortices are not stable to spanwise perturbations. During the linear development of the dominant Görtler vortices, vortices with other wavelengths grow independently at the rate given by primary instability at these wavelengths. As the dominant Görtler vortices develop into the nonlinear stage, spatial Eckhaus instability sets in. The nonlinear growth of this instability can generate new vortices or cause some dominant Görtler vortices to disappear. Since the dominant Görtler vortices break down shortly after they enter nonlinear stage, we do not expect splitting and merging of vortices to affect the wavelength selection process significantly. Instead, they will deform the dominant Görtler vortices significantly and produce irregular vortices. We believe this explains the prevailing irregularities of Görtler vortices observed experimentally.

Compared to Dean vortices, the interactions between Görtler vortices with different wavelengths are relatively weak. Our simulations show that the interactions alone do not change the wavelengths of the vortices significantly, but they do modify the structures of the Görtler vortices and generate irregularity.

7. Concluding remarks

This study shows that spatially developing Dean vortices and Görtler vortices are unstable to spanwise perturbations. This instability is mostly characterized by vortex splitting and merging in a channel geometry, and by irregular vortex structures in a concave boundary layer. If there were no such instability, then when vortices of a

certain wavelength become nonlinear, all disturbances with other wavelengths would decay. This would result in regular symmetric nonlinear vortices (like those observed in Taylor–Couette flow where the stable region of a similar instability is a large open region, cf. Riecke & Paap 1986), and the irregular non-symmetric vortex structures observed in curved channel and concave boundary layer experiments would not occur.

The study done by Guo & Finlay (1991) shows that in the context of temporal theory, the streamwise vortices caused by rotation or by both rotation and streamwise curvature in channel geometries have an Eckhaus instability similar to that of Dean vortices. Vortex splitting and merging phenomenon are also observed in cross-flow vortices (Spalart 1989; Bippes 1992, personal communication). Whether the features of Dean and Görtler vortices found in this study exist for vortices caused by rotation in a rotating channel or on a rotating flat plate, or those caused by cross-flow instability remains to be seen. Since the nonlinear development of this type of instability modifies the vortex structures significantly (in both Dean and Görtler problems), the study of this type of instability and its effects on the onset of other secondary instabilities is a necessary step toward understanding the transition to turbulence.

REFERENCES

AIHARA, Y. & KOYAMA, H. 1980 Secondary instability of Görtler vortices: formation of periodic three-dimensional coherent structure. *Trans. Japan Soc. Aero. Astron.* **24**(64), 78–94.

AIHARA, Y., TOMITA, Y. & ITO, A. 1984 Generation, development and distortion of longitudinal vortices in boundary layers along concave and flat plates. In *Laminar–Turbulent Transition, IUTAM Symp., Novosibirsk, 1984* (ed. V. V. Kozlov), pp. 447–454.

ALFREDSSON, P. A. & PERSSON, H. 1989 Instabilities in channel flow with system rotation. *J. Fluid Mech.* **202**, 543–557.

BAKER, A. J. 1983 *Finite Element Computational Fluid Mechanics*. McGraw-Hill.

BARA, B., NANDAKUMAR, K. & MASLIYAH, J. H. 1992 An experimental and numerical study of the Dean problem: flow development towards two-dimensional, multiple solutions. *J. Fluid Mech.* **244**, 339–376.

BERTOLOTTI, F. P., HERBERT, TH. & SPALART, P. R. 1992 Linear and nonlinear stability of the Blasius boundary layer. *J. Fluid Mech.* **242**, 441–474.

BIPPES, H. 1972 Experimentelle Untersuchung des laminar–turbulenten Umschlags an einer parallel angeströmten konkaven wand. *Sizungsberichte der Heidelberger Akademie der Wissenschaften Mathmatisch-naturwissenschaftliche Klasse, 3 Abhandlund, Jahrgang 1972*, pp. 103–180; also *NASA TM*. 75243, 1978.

BOTTARO, A. 1993 On longitudinal vortices in curved channel flow. *J. Fluid Mech.* **251**, 627–660.

BOTTARO, A., MATSSON, O. J. E. & ALFREDSSON, P. H. 1991 Numerical and experimental results for developing curved channel flow. *Phys. Fluids* A **3**, 1473–1476.

DAY, H. P., HERBERT, TH. & SARIC, W. S. 1990 Comparing local and marching analyses of Görtler instability. *AIAA J.* **28**, 1010–1015.

DEAN, W. R. 1928 Fluid motion in a curved channel. *Proc. R. Soc. Lond.* A **121**, 402–420.

DRAZIN, P. G. & REID, W. H. 1981 *Hydrodynamic Stability*. Cambridge University Press.

ECKHAUS, W. 1965 *Studies in Nonlinear Stability Theory*. Springer.

FINLAY, W. H., KELLER, J. B. & FERZIGER, J. H. 1988 Instability and transition in curved channel flow. *J. Fluid Mech.* **194**, 417–456.

FLETCHER, C. A. J. 1988 *Computational Techniques for Fluid Dynamics*, Vol. II. Springer.

FLORYAN, J. M. & SARIC, W. S. 1984 Wavelength selection and growth of Görtler vortices. *AIAA J.* **22**, 1529–1538.

GÖRTLER, H. 1940 Uber eine driedimensionale instabilitat laminarer Grenzshichten an konkaven wanden. *Math. Phys.* Kl **2**, 1; also *NASA TM* 1375 (1954).

GUO, Y. 1992 Spanwise secondary instability of Dean & Görtler vortices. PhD thesis, University of Alberta.

GUO, Y. & FINLAY, W. H. 1991 Splitting, merging and wavelength selection of vortices in curved and/or rotating channel flow due to Eckhaus instability. *J. Fluid Mech.* **228**, 661–691.

HALL, P. 1983 The linear development of Görtler vortices in growing boundary layers. *J. Fluid Mech.* **130**, 41–58.

HALL, P. 1988 The nonlinear development of Görtler vortices in growing boundary layers. *J. Fluid Mech.* **193**, 243–266.

HALL, P. 1990 Görtler vortices in growing boundary layers: the leading edge receptivity problem, linear growth and the nonlinear breakdown stage. *Mathematika* **37**, 151–189.

HERBERT, TH. 1976 On the stability of the boundary layer along a concave wall. *Arch. Mech. Stos.* **28**, 1039–1055.

HERBERT, TH. 1988 Secondary instability of boundary layers. *Ann. Rev. Fluid Mech.* **20**, 487–526.

KLEISER, L. & SCHUMANN, U. 1984 Spectral simulation of the laminar turbulent transition process in plane Poiseuille flow. In *Spectral Methods for Partial Differential Equations* (ed. R. G. Voigt, D. Gottlieb & M. Y. Hussaini), p. 141. SIAM.

LEE, K. & LIU, J. T. C. 1992 On the growth of mushroom-like structures in nonlinear spatially developing Görtler vortex flow. *Phys. Fluids* A **4**, 95–103.

LIGRANI, P. M., LONGEST, J. E., FIELDS, W. A., KENDALL, M. R., FUQUA, S. J. & BAUN, L. R. 1992 Initial development and structure of Dean vortex pairs in a curved rectangular channel including splitting, merging and spanwise wavenumber selection. *Phys. Fluids* A submitted.

LIGRANI, P. & NIVER, R. D. 1988 Flow visualization of Dean vorties in a curved channel with 40 to 1 aspect ratio. *Phys. Fluids* **31**, 3605–3618.

LIU, W. & DOMARADZKI, J. 1990 Direct numerical simulation of transition to turbulence in Görtler flow. *AIAA Paper* 90-0114.

MADAY, Y. & PATERA, A. T. 1989 Spectral element methods for the incompressible Navier–Stokes equations. In *State-of-the-Art Surveys on Computational Mehanics* (ed. A. T. Noor & J. T. Oden), pp. 71–143. ASME.

MATSSON, O. J. E. & ALFREDSSON, P. H. 1990 Curvature- and rotation-induced instabilities in channel flow. *J. Fluid Mech.* **202**, 543–557.

MATSSON, O. J. E. & ALFREDSSON, P. H. 1992 Experiments on instabilities in curved channel flow. *Phys. Fluids* A **4**, 1666–1676.

PATANKAR, S. V. & SPALDING, D. B. 1972 A calculation procedure for heat, mass and momentum transfer in three-dimensional parabolic flows. *Intl J. Heat Mass Transfer* **15**, 1787–1806.

PATERA, A. T. 1984 A spectral element methods for fluid dynamics: laminar flow in a channel expansion. *J. Comput. Phys.* **54**, 468–488.

RIECKE, H. & PAAP, H. 1986 Stability and wave-vector restriction of axisymmetric Taylor vortex flow. *Phys. Rev.* A **33**, 547–553.

RØNQUIST, E. M. 1988 Optimal spectral element methods for the unsteady three-dimensional incompressible Navier–Stokes equations. PhD thesis, Massachusetts Institute of Technology.

RUBIN, S. G., KHOSLA, P. K. & SAARI, S. 1977 Analysis of global pressure relaxation for flows with strong interaction and separation. *Computers Fluids* **11**, 281–306.

SABRY, A. S. 1988 Numerical computation of the nonlinear evolution of Görtler vortices. PhD thesis, Brown University.

SABRY, A. S. & LIU, J. T. C. 1991 Longitudinal vorticity elements in boundary layers: nonlinear development from initial Görtler vortices as a prototype problem. *J. Fluid Mech.* **231**, 615–663.

SCHLICHTING, H. 1955 *Boundary-Layer Theory*. McGraw-Hill.

SPALART, P. R. 1989 Direct numerical study of crossflow instability. In *Laminar–Turbulent Transition IUTAM Symp. Toulouse/France 1989* (ed. D. Arnal & R. Michel), Springer.

SWEARINGEN, J. D. & BLACKWELDER, R. F. 1987 The growth and breakdown of streamwise vortices in the presence of a wall. *J. Fluid Mech.* **182**, 255–290.

TANI, I. 1962 Production of longitudinal vortices in the boundary layer along a curved wall. *J. Geophys. Res.* **67**, 3075–3080.

WINOTO, S. H. & CRANE, R. I. 1980 Vortex structure in laminar boundary layers on a concave wall. *Intl J. Heat Fluid Flow* **2**, 221–231.

YANG, K. S. & KIM, J. 1991 Numerical investigation of instability and transition in rotating plane Poiseuille flow. *Phys. Fluids* A **3**, 633–641.

YU, X. Y. & LIU, J. T. C. 1991 The secondary instabilities in Görtler flow. *Phys. Fluids* A **3**, 1845–1847.